Geophysical Journal International

Geophys. J. Int. (2012) **189,** 1681–1700 doi: 10.1111/j.1365-246X.2012.05442.x

Multistep modelling of receiver-based seismic and ambient noise data from WOMBAT array: crustal structure beneath southeast Australia

Hrvoje Tkalčić,[1] Nicholas Rawlinson,[1] Pierre Arroucau,[1,2] Amarjeet Kumar[1,3,*] and Brian L. N. Kennett[1]

[1]*Research School of Earth Sciences, The Australian National University, Mills Road, Building* 61*, Canberra ACT* 0200*, Australia.*
E-mail: Hrvoje.Tkalcic@anu.edu.au
[2]*Center for Research Excellence in Science and Technology, North Carolina Central University, Durham, NC* 27707*, USA*
[3]*Indian Institute of Technology, Kharagpur, West Bengal* 721302*, India*

Accepted 2012 March 2. Received 2012 March 2; in original form 2011 September 11

SUMMARY

A limitation of most forms of passive seismic tomography using distant earthquakes lies in the fact that crustal structure is poorly resolved. An attempt is made here to address this issue by modelling teleseismic receiver functions (RFs) and dispersion curves derived from ambient noise through a multistep approach. The SEAL3 experiment in central and southern New South Wales (NSW) used here, represents one of 13 array deployments that so far comprise the large WOMBAT project, which aims to cover a significant portion of the Australian continent with a rolling array of seismometers.

An interactive, forward-modelling software package (IRFFM2) is introduced and applied to the observed RFs and surface wave dispersion curves to define a prior, physically acceptable range of elastic parameters in the lithosphere, which is combined with a grid-search and a linearized inversion.

Our results emphasize the importance of a joint treatment of RFs and dispersion data as the predictions from 1-D velocity models at individual stations derived from only RFs display large departures from the observed ambient noise dispersion curves. In total, 27 jointly constrained 1-D shear wave models are produced, which provide sufficient sampling of the crust beneath SEAL3 to permit detailed inferences about lateral variations in structure to be made. Of particular note is the observation that the Moho deepens towards the mountainous southeast, where it exceeds 50 km in depth beneath the Southern Highlands of NSW, thus marking out some of the thickest crust in Australia. The complex lateral variations in mid-lower crustal velocity that we observe probably reflect the manifold interactions of a thinning lithosphere, associated igneous underplating, recent hot-spot-related volcanism and uplift. Our results image an important part of the lithosphere that is poorly constrained by regional and teleseismic tomography, and contribute to the understanding of the formation of the southern highlands and the Palaeozoic Lachlan Orogen.

Key words: Time-series analysis; Composition of the continental crust; Cratons.

1 INTRODUCTION AND MOTIVATION

1.1 Teleseismic receiver-functions modelling and beyond

Receiver functions (RFs) technique has been widely used in seismology to probe Earth's lithospheric structure. The technique takes advantage of repetitive waveform features of three-component seismograms and isolates the shear wave response of the crust and upper mantle beneath the recording station. Ever since the pioneering work of Phinney (1964), the method has been constantly improving, but more innovations are required as the simplicity of our assumptions is rarely a match for the formidable complexity of Earth structure. The advantages and disadvantages of the technique are described in some of the early papers (e.g. Langston 1979; Owens 1987; Ammon *et al.* 1990; Cassidy 1992). Different styles of transformations of coordinates have been used to determine structure from the inversion of RFs, including those that minimize the initial *P*-pulse (e.g. Vinnik 1977; Kind *et al.* 1995; Reading *et al.* 2003). It is common to perform the deconvolution of an incident wave from the mode-converted wave in either the frequency (e.g. Langston 1979; Owens

*Now at: Delphi Consortium, TU-Delft University, Stevinweg 1, 2628 Delft, the Netherlands.

© 2012 The Authors
Geophysical Journal International © 2012 RAS

et al. 1987; Ammon 1991; Park & Levin 2000; Helffrich 2006) or the time domain (e.g. Ligorría & Ammon 1999; Julià *et al.* 2000).

Methods to minimize the objective function (related to RFs time-series) have relied on forward modelling (e.g. Baker *et al.* 1996; Çakir *et al.* 2000; Zhu & Kanamori 2000), linearized inversion (e.g. Ligorría & Ammon 1999), grid-search (e.g. Sandvol *et al.* 1998) or a combination of approaches (Tkalčić *et al.* 2006). Non-linear techniques such as the genetic algorithm (Shibutani *et al.* 1996), the neighbourhood algorithm (Sambridge 1999; Agostinetti *et al.* 2002), the microgenetic algorithm (Chang *et al.* 2004) and the niching genetic algorithm (Lawrence & Wiens 2004) have also been widely used. Although inversion is a dominant method for interpreting RFs, we have recently developed interactive software for forward modelling of RFs—Interactive Receiver Function Forward Modeller (IRFFM; ref. Tkalčić *et al.* 2011) that allows a quick assessment of different features seen in the observed RFs. Interactive modelling also enables a rapid exploration of a wide range of 1-D velocity models and provides an instant intuitive insight on feasible elastic parameters in the earth models.

There are a large number of studies that use RFs and produce a first-order estimate of structural models of Earth, with parameters such as crustal thickness. However, methods that use multiple overlapping geophysical data have the advantage of improved sensitivity to absolute velocities, compared to RFs alone (e.g. Özalaybey *et al.* 1997; Du & Foulger 1999; Julià *et al.* 2000, 2003; Pasyanos *et al.* 2007). Using several geophysical data sets to increase constraints on Earth structure is, arguably, a problem best approached through a multistep method such as that described in Tkalčić *et al.* (2006) and Tkalčić *et al.* (2011). The multistep method integrates grid-searches, forward-modelling and inversion schemes. Fragmentation of data analysis to a number of steps allows the modeller to get an intuitive knowledge of how each part of the earth model responds to a particular data set. Here we consider RFs and complement them with the Rayleigh wave group velocity dispersion curves obtained through an analysis of ambient noise.

In this study, we introduce and make freely available an extension of IRFFM tool—Simultaneous Receiver Functions and Surface Wave Dispersion Forward Modeller (IRFFM2), a forward-modelling tool that enables simultaneous modelling of RFs and surface wave dispersion curves (Tkalčić 2011). IRFFM2 is used at various stages of our analysis. For example, the best fit to the observed RFs is first found using IRFFM2 with a small number of free parameters. This model is then further refined through a linearized inversion. IRFFM2 is used again to find a reasonable simultaneous fit to the observed RFs and the Rayleigh wave group velocity dispersion from the ambient noise. The updated model from this process is then used as a starting model in a joint linearized inversion. We show that for a study of 1-D structure, it is pertinent (whenever possible) to use at least two independent geophysical data sets to help overcome the non-uniqueness of the solution, although, arguably, wide-range angle data could constrain 1-D velocity and interface depth.

1.2 Receiver-based studies in Australia

The Research School of Earth Sciences at the Australian National University has invested significant efforts over the years in deploying and maintaining continental seismic stations and arrays, consisting of both broad-band and short-period instruments (http://rses.anu.edu.au/seismology/seismology_map/). Of a significant number of temporary stations, more than 500 short-period instruments have been installed in southeast Australia during the last decade, with an average spacing of about 50 km (e.g. SEAL, Rawlinson *et al.* 2006; EVA, Rawlinson & Kennett 2008). These stations were installed as part of 13 sequentially deployed arrays that comprise the current state of the WOMBAT transportable array experiment (Rawlinson *et al.* 2008). WOMBAT's objective is to cover a significant part of the Australian continent and enable detailed seismic studies, including tomography and other receiver-based techniques. One of the anticipated goals is to resolve small-scale structural features, which enables the construction of a new Australian Moho model with unprecedented 0.5° resolution. This will allow the augmentation and further development of global crustal models (e.g. Laske *et al.* 2000).

The most detailed study from teleseismic RFs of the crustal thickness of the Australian continent so far (Clitheroe *et al.* 2000) used data from temporary broad-band stations from the Skippy (van der Hilst *et al.* 1994) and Kimba (Kennett 1997) deployments. Chevrot & van der Hilst (2000) introduced a method for a domain search of crustal thicknesses and v_p/v_s ratio and did a comprehensive study of the Poisson ratio of the Australian crust. The study of Clitheroe *et al.* (2000) confirmed earlier work of Drummond & Collins (1988) and Collins (1991), who found from seismic refraction and reflection data that the Lachlan Fold Belt (mountain belt in Fig. 1) is a region with some of the thickest crust in Australia.

SEAL3, the ninth WOMBAT deployment, consists of three-component short-period LE3Dlite seismometers with a corner frequency of 1 Hz deployed for between 9 and 15 months duration. In total, there are 57 stations spaced between 45 and 55 km apart that occupy the eastern and central subprovinces of the Lachlan Fold Belt located in New South Wales (Figs 1 and 2). Although, the southeast Australia has some of the highest population density in Australia, a number of SEAL3 stations are located in the Australian Outback, in very remote areas of the continent. This is a poorly understood region of the Australian crust, and the advent of the SEAL3 data set will contribute to an improved understanding of the tectonic setting of the Lachaln Orogen.

Here we augment previous coverage with 27 new locations and perform a comprehensive point measurement of lithospheric structure properties under each site. A dense spatial coverage of instruments is of particular interest as it can be used for collecting a variety of independent seismic data sets that together constrain, *inter alia*, the full thickness of the crust. Our analysis yields an additional level of local complexity of crustal thickness, and confirms a deep Mohorovičić discontinuity (Moho; Mohorovičić 1910) near the coastline, with a gradual thinning of the crust towards central NSW, where Moho lies at about 35–38 km depth. These results will be important for the improvement of seismic tomography and the interpretation of lithospheric processes on a wider scale, when more profiles from the surrounding deployments become available.

1.3 Crustal structure beneath southeast Australia

The evolution of the Australian continent spans a broad geologic time scale, with the formation of the Yilgarn Craton in Western Australia beginning well before 3.5 Ga (Betts *et al.* 2002). In fact, detrital zircons as ancient as 4.4 Ga have been found in the Yilgarn province, and represent the earliest evidence for continental crust and oceans on Earth (Wilde *et al.* 2001). By contrast, recent Quaternary hotspot volcanism in the Newer Volcanic Provinces of southeast Australia has seen the formation of basaltic lava fields as young as 10 ka (Price *et al.* 1997). The Australian continent really only began to take shape during the Proterozoic, with elements of the north (including the Kimberley Craton and Arunta Block),

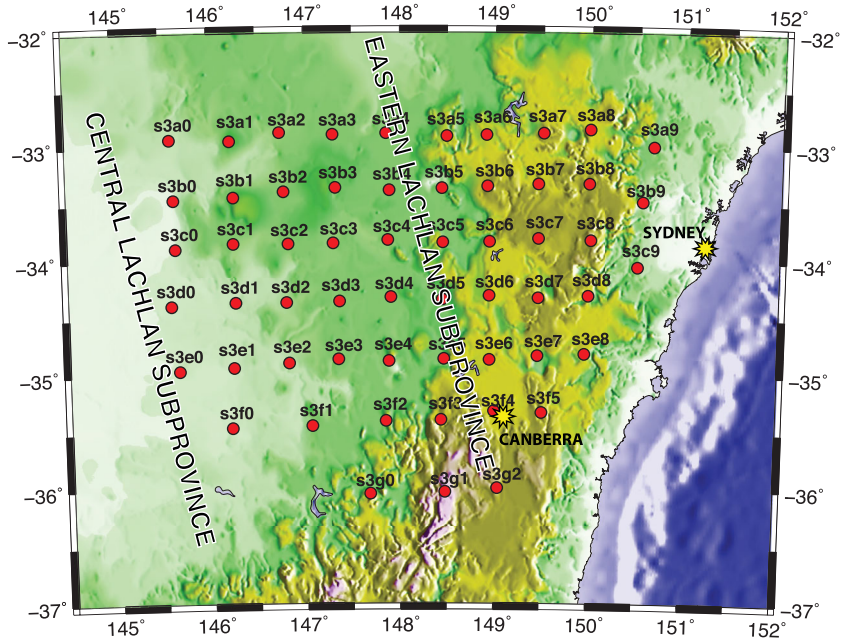

Figure 1. Topographic map of the region occupied by the SEAL3 stations used in this study.

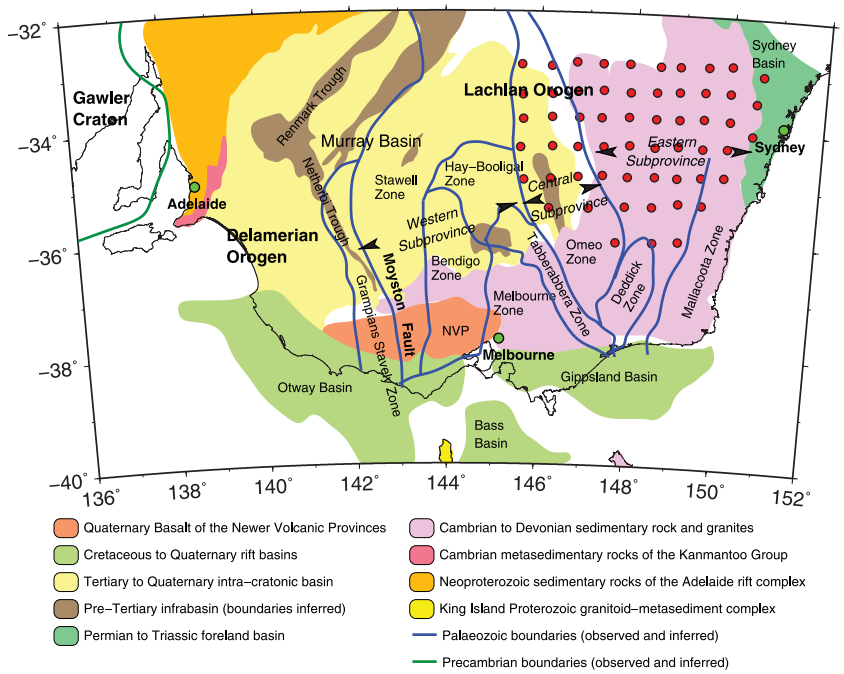

Figure 2. Simplified map showing broad-scale surface geology and inferred Palaeozoic boundaries in southeast Australia. The red dots denote the locations of the SEAL3 stations.

south (including the Gawler and Curnamona cratons) and west (including the Yilgarn and Pilbara cratons) amalgamating as a result of both accretionary processes and continent–continent collision (Betts *et al.* 2002). The eastern third of Australia, often known as the Tasmanides or Tasman Fold Belt, largely formed between the Middle Cambrian and Middle Triassic (Glen 2005), and consists of a series of outward stepping accretionary orogens that developed during the easterly retreat of the palaeo-Pacific Plate (Glen *et al.* 2009). In southeast Australia, the Delamerian Orogen began to form along the eastern margin of Gondwana in the Middle Cambrian, followed in the Late Cambrian by the Lachlan Orogen (Fig. 2).

Foster *et al.* (2009) separate the Lachlan Orogen into three subprovinces (see Fig. 2)—the Western, Central and Eastern—which correspond to separate thrust systems. The Western Subprovince is an east-vergent thrust system, the Central Subprovince comprises a SW-vergent thrust belt and features a high temperature, low pressure metamorphic complex (in the Omeo Zone; see Fig. 2) and the Eastern Subprovince contains of a number of west-dipping fault zones, and incorporates the Ordovician Macquarie Arc, which was accreted by a combination of thick- and thin-skinned thrusting. Following the formation of the Lachlan Orogen in the Palaeozoic, the Mesozoic break-up of Gondwana led to the development of passive

margins to its south and east. The break-up of Australia and Antarctica, which began at ∼160 Ma, resulted in the formation of the Bass, Otway and Gippsland basins (Fig. 2). Uplift along the eastern margin, which began in the Cretaceous and continued into the Tertiary, appears to coincide with onshore volcanism, possibly linked to mafic underplating (Betts *et al.* 2002). This is consistent with the formation of an upper plate passive margin (Lister *et al.* 1991). However, the role played by the opening of the Tasman Sea in the formation of the south-eastern highlands of Australia (see Fig. 2) is a matter of much debate, with other models (van der Beek *et al.* 1999) suggesting that the current highlands are an erosional remnant of a much larger mountain belt associated with late Palaeozoic orogenies.

As well as the Otway, Bass and Gippsland basins, the Palaeozoic basement of the Lachlan Orogen is also obscured by the vast intracratonic Murray Basin (see Fig. 2), which is composed of a thin layer of marine Tertiary sediments overlain by a complex of fluvial and aeolian Quaternary sediments (Knight *et al.* 1995). Evidence from potential field data and drilling points to the presence of several pre-Tertiary infrabasins concealed beneath the Murray Basin. Further east, the Sydney Basin, a foreland basin from Permian–Triassic, masks a relatively small portion of the Eastern Subprovince of the Lachlan Orogen. The presence of these Mesozoic–Cenozoic cover sequences have contributed to the difficulty of trying to unravel the tectonic evolution of ancient orogenies in southeast Australia. Currently, most models can be separated into two distinct classes: those that appeal to accretionary oceanic systems involving multiple coeval subduction zones (e.g. Foster & Gray 2000), and those that involve orogen-parallel transport (e.g. Taylor & Cayley 2000). Consequently, the origin of the underlying lithosphere may vary between purely oceanic, to mixed oceanic and continental (Glen 2005). It has also been recognized that fragments of Precambrian continental lithosphere set adrift by the break-up of the supercontinent Rodinia may have become incorporated within the Lachlan Orogen (Cayley *et al.* 2002).

2 MULTISTEP METHOD IN MODELLING RFs FROM TELESEISMIC EARTHQUAKES AND RAYLEIGH WAVE DISPERSION CURVES FROM AMBIENT NOISE

2.1 Pre-processing of raw waveforms

The raw waveform data are converted to a continuous 'miniseed' format and events with $M_b \geq 5.5$ whose epicentral distances are confined between 30° and 90° from a recording station were extracted to secure near-vertical incidence of the *P* waves. For the time period of SEAL3 operation, this yielded about 120 teleseismic events on average per station. The distribution of all 57 stations used in this study is shown in Fig. 1. Most seismicity that occurred at distances suitable for the RFs technique is confined to Indonesia in the north and northwest, and to the Tonga–Fiji region in the northeast. There is also a group of earthquakes that occurred in the Indian Ocean, resulting in the western backazimuths, and some events originating south of Australia and in the New Zealand region with southern backazimuths. Because of limited operation time and the fact that a single station collects a large number of potentially useful teleseismic events, at this stage we do not perform strict data-quality control on the raw waveforms, apart from the criterion that their M_b must be larger than 5.4. We remove the mean and trends, and apply a series of high-pass and bandpass filters, mostly to eliminate long-period noise and increase signal-to-noise ratio of later arrivals corresponding to crustal reverberations. We choose a filter producing the best signal-to-noise ratio and most coherent RFs for each station. A high-pass filter with a corner frequency 0.5 Hz produces good results at most stations. We then extract a 25-s long time-series concentrating on the first arrival by cutting traces at 5 s before and 20 s after the initial *P*-wave arrival. Finally, horizontal components are rotated to radial and tangent directions before iterative deconvolution is applied to the waveforms, with the Gaussian parameter $a = 2.5$ (Ligorría & Ammon 1999).

We divide waveform data in the reference frame of each station based on their directions of sampling (backazimuth of their incoming energy) to four major quadrants, each quadrant corresponding to 90° bandwidth of the backazimuthal range. The first quadrant encompasses backazimuths between 0° and 90°, and the consecutive quadrants are defined in the clockwise direction. In general, for the analysed stations there is a very small and insignificant number of RFs for earthquakes corresponding to the second and the third quadrants (south-western and south-eastern backazimuths). A further step in pre-processing RFs is the selection of a subset of RFs with a very similar range of backazimuths and ray parameters. The data from the first quadrant (Tonga–Fiji) show more coherency than the data from the fourth quadrant (Indonesia), which is likely because of different orientation of tectonic plates and radiated *P*-wave energy towards Australia. Also, it has been shown that the waves arriving to Australia from the northern azimuths experience very high intrinsic quality factor *Q* (low intrinsic attenuation) and multiple scattering because of heterogeneities in the lower crust and mantle, and that they can have very long high-frequency coda (Kennett & Furumura 2008). By choosing a narrow azimuthal range and a narrow interval of ray parameters, we neglect possible Moho dip and anisotropy, but these are, arguably, only second-order effects in the context of meeting our goal of deriving 1-D models of the crust and upper mantle that are compatible with multiple geophysical data sets.

Working with a small to moderate number of RFs usually allows us to select waveforms for stacking by visual examination for their coherency in *P–S* conversions, and to carefully eliminate outliers and noisy records. When the number of RFs in a bundle is large, it becomes challenging to justify a visual selection of waveforms for stacking. One cannot rely on automated high signal-to-noise ratio picking, because in cases where the first arrivals are misidentified, the signal-to-noise ratio might still be favourable, but the corresponding waveform might be different from the rest of the waveforms in a bundle. An *ad hoc* determination of outliers that should be discarded before stacking is also not desirable, because a subjective selection of the waveforms for stacking can result in an averaged waveform that is distorted or lacking some representative features, especially at the later times where the signals from the changes in crustal properties are weaker. Therefore, we select mutually coherent waveforms and stack them following the cross-correlation matrix approach described in Tkalčić *et al.* (2011) and used in Chen *et al.* (2010). This results in an averaged RF and additional statistical information about highly correlated waveforms chosen for stacking. Our strict criteria yield reliable RFs at 27 of the 57 stations of SEAL3 deployment. More details describing the pre-processing of RFs are given in Tkalčić *et al.* (2011).

2.2 IRFFM2—interactive forward modelling (Steps 1 and 4)

The IRFFM is a Java program written for interactive forward modelling of RFs assuming horizontal isotropic and homogeneous layers. The software has been made freely available via the Internet (Tkalčić *et al.* 2011). It has been used as a complement to inversion modelling or as a stand-alone tool (Stipčević *et al.* 2011; Young *et al.* 2012). Here we introduce the IRFFM2 and use it in Step 1 as well as in Step 4 of our multistep method (see Fig. 3). As with IRFFM, an easy-to-use graphic interface is designed to enable the user to efficiently manipulate the thicknesses and velocities of the layers, as well as v_p/v_s ratios in a 1-D model of Earth. The display quickly shows the theoretical versus the observed RFs and surface wave dispersion (it is possible to simultaneously model all four instances of Rayleigh and Love wave group and phase velocities) and reveals how the 1-D model has to be changed to reduce their misfit. The input RF, dispersion and velocity models are in 'ASCII' format, and two starting models are provided with the package (ak135, Kennett *et al.* 1995 and PREM, Dziewonski & Anderson 1981). The users can identify one of these two models as a starting model, construct their own starting models from other geophysical constraints or simply guess an initial Earth structure. It is possible to save the current model at any time during the forward modelling for future use, or upload another observed RF and dispersion data at any time. It is also possible to save the current result as a graphical image or send it to the printer.

The method used in IRFFM2 for the forward calculation of the theoretical RFs consists of the synthetic seismogram algorithm by G. Randall (*respknt*), based on the method developed by Kennett (1983) and a time domain deconvolution to produce synthetic RFs in the same manner as it is done for the observed RFs (*iterdecon*). The forward method used to calculate dispersion is DISPER80 developed by Saito (1988).

We use IRFFM2 to get a quick understanding of the features present in the RF waveforms, as well as a quantitative estimate of the range of free parameters (thicknesses and velocities of the layers) that produce reasonable fit to the observed RFs (Step 1). In Step 1, we fit only RFs and disregard the dispersion information. One can quickly explore how the crustal thickness and the impedance contrast affect the *P* to *S* conversion, seen as the second peak in the observed RFs. One can also get a feeling for the number of layers needed to produce the observed complexity of the RFs. The parameter space that is determined as a result of Step 1 is then used as *a priori* information for a grid-search that explores structural models of Earth in a more systematic way (Step 2). Similarly, the resulting models determined through IRFFM2 in the simultaneous forward modelling (Step 4) are used as starting models in the linearized joint inversion of RFs and the Rayleigh wave group velocity dispersion (Step 5). A screenshot of the IRFFM2 user interface is shown in Fig. 4. This figure illustrates how Earth structure is modelled starting with only two layers in the crust (as in ak135, Kennett *et al.* 1995), which were gradually split and expanded to more layers and their thicknesses and velocities were changed to fit the observed RF and Rayleigh wave group velocity dispersion at station S3B5. In this example, v_p/v_s ratio along the profile is kept constant (i.e. equal to 1.73), although it can be variable. The estimated model parameters using IRFFM2 are coarse, but, in general, the Step 1 models do not deviate significantly from the models established after Step 3 based on RFs only (some models are shown in Figs 6 and 8 with orange lines) and the Step 4 models do not deviate much from our final models (after Step 5) based on a linearized joint inversion (shown with red lines in Figs 6, 8 and 9). IRFFM and IRFFM2 are available for download from the following Internet address: www.rses.anu.edu.au/h̃rvoje/IRFFM.html. (IRFFM2 will be released simultaneously with the publication of this manuscript.)

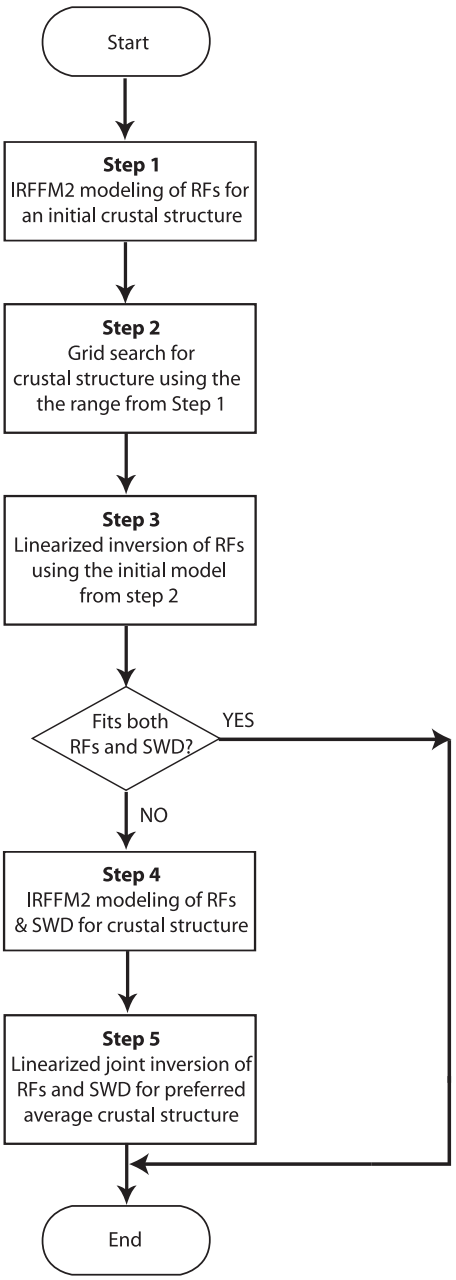

Figure 3. A flowchart demonstrating the multiple steps of the method.

2.3 Grid-search for first-order lithospheric structure (Step 2)

The main benefit of using IRFFM2 (Step 1) is to allow a rapid assessment of the principal details beneath the station of interest (such as the position and sharpness of Moho). Once the initial estimates of 1-D structure beneath each of the 27 stations are made, we can make further improvements to 1-D structure by using a grid-search method. Although time consuming and limited by its discrete nature, a critical advantage of a grid-search method over

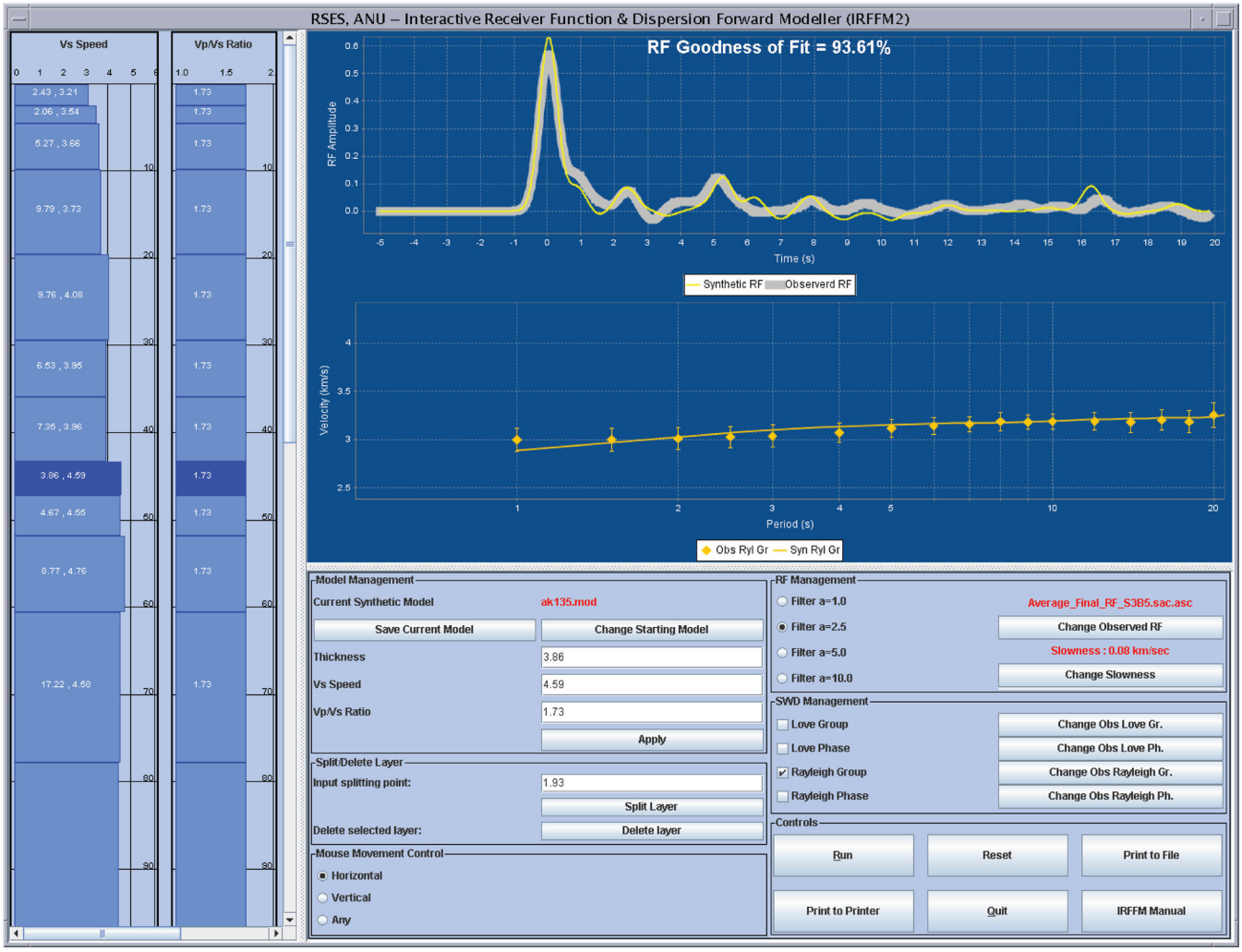

Figure 4. A snapshot of interactive forward modelling of data from station S3B5 using IRFFM2 (Steps 1 and 4). Observed radial RF (grey thick line) and Rayleigh wave group velocity dispersion (yellow diamonds with error bars) are modelled starting with ak135 (Kennett *et al.* 1995), adding more layers, and changing their thicknesses and velocity (left). Yellow lines represent theoretical RF and dispersion curve corresponding to the 1-D model shown in left. Here, the layers in the crust were modelled for thickness and *S*-wave velocity, keeping v_p/v_s ratio 1.73.

Table 1. Grid-search scheme used in the study, with flexible depth of the Moho defined between 24 and 48 km.

Layer	Thickness (km)	v_s (km s^{-1})	Δh (km)	Δv (km s^{-1})
1	$H_1 = 2$–6	$V_1 = 2.8$–3.6	2	0.2
2	$H_2 = 3 - H_{moho} - (H_1 + H_3 + H_4)$	$V_2 = 3.2$–3.6	3	0.2
3	$H_3 = 3 - H_{moho} - (H_1 + H_2 + H_4)$	$V_3 = 3.4$–3.8	3	0.2
4	$H_4 = 3 - H_{moho} - (H_1 + H_2 + H_3)$	$V_4 = 3.6$–4.5	3	0.3
5	$H_5 = 80 - H_{moho}$	$V_5 = 4.4$–4.6	–	0.1

other inversion techniques is that it provides goodness-of-fit statistics for the entire parameter space. This could be advantageous in situations where not even an approximate structure under a station is known *a priori*.

We use the grid-search scheme as defined in Tkalčić *et al.* (2006, 2011). The grid specifications are shown in Table 1. The inverse problem is reduced to four layers in the crust and a layer in the mantle extending to the depth of 80 km. Below 80 km, we use a series of layers with thicknesses and velocities from PREM (Dziewonski & Anderson 1981). We assume Poisson's ratio of $\sigma = 0.25$ and Birch's law for density (Birch 1961). We first impose minimal *a priori* constraints on crustal thickness from the interactive forward modelling described in the previous section, and allow it to vary between 24 and 48 km, and in some cases from 33 to 57 km. This is a relatively broad range of thicknesses and adds to the computational expense, however, it is within an interval of crustal thicknesses predicted by previous studies (e.g. Drummond & Collins 1988; Clitheroe *et al.* 2000). The grid points are separated by 2 km for surface layer thickness, 3 km for other layers and encompass shear wave velocity intervals that differ by 0.2–0.3 km s^{-1} depending on the depth of the layers. The number of free parameters for four crustal layers and one mantle layer thus equals $2n + 1 = 9$, where n is the number of layers (the factor 2 comes from shear wave velocity and thickness of each layer, and an additional free

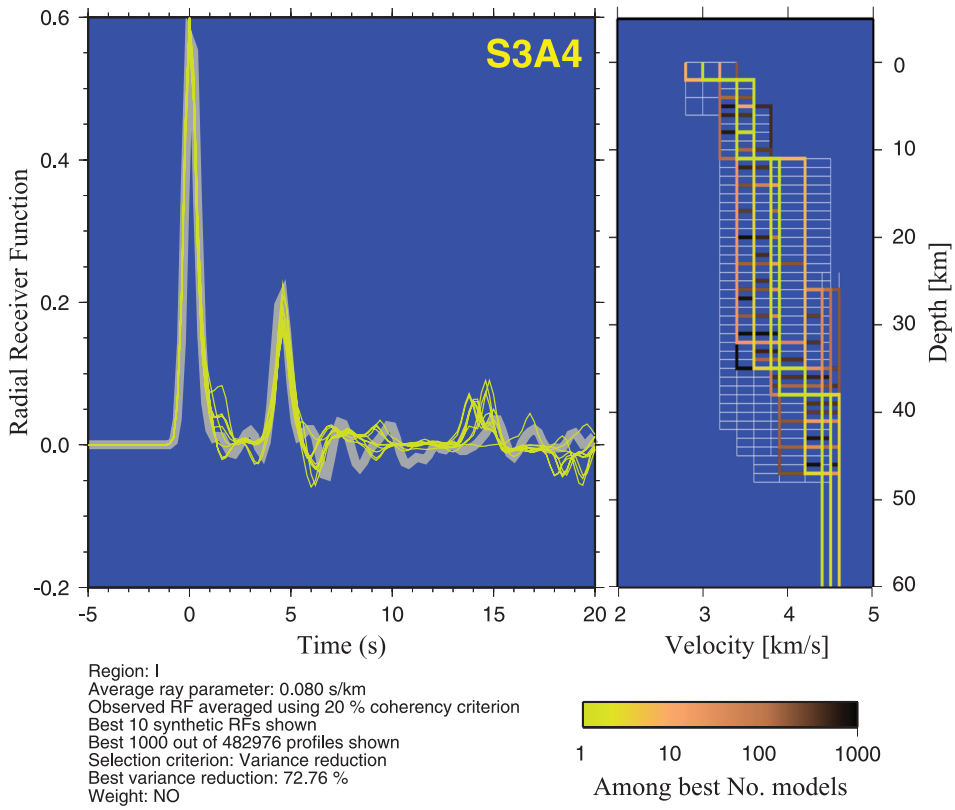

Figure 5. An example of an intermediate result of modelling of Earth structure beneath station S3A4 after Step 2 (grid-search for four layers in the crust and a half-space in the uppermost mantle; see Table 1). On the left, the observed RF is shown with thick grey line, and the synthetic RFs from the best 10 models are shown with yellow thin lines. On the right, best-fitting 1000 models are shown using the logarithmic colour scheme from yellow to dark brown. Thin grey lines indicate the background grid.

parameter is the shear wave velocity of the layer extending to the depth of 80 km). We compute and store a database of synthetic RFs from a suite of models according to the scheme above: this results in 482 976 synthetic RFs for each ray parameter. To compute synthetic RFs, we use the same method as in the forward approach with IRFFM2 using a Gaussian filter-width parameter $a = 2.5$ and the duration of 25 s, for a range of ray parameters. Additional details of how the measure of misfit, that is variance reduction (VR) for each model is calculated can be found in Tkalčić *et al.* (2006, 2011).

An example of a grid-search result for station S3A4 is shown in Fig. 5. The best thousand models and the explored grid are shown on the right-hand side of the figure, with a logarithmic colour scheme emphasizing the best 10 models in yellow. Synthetic RFs for these 10 best models are also shown and compared to the observed RF on the left-hand side of the figure. Given that only four layers in the crust are allowed, the fits are reasonably good, yielding VR higher than 70 per cent. The models obtained here are already an accurate representation of average crustal structure in terms of the position of the main velocity gradients, but as we will show, it is important to also fit other available data when deriving final 1-D velocity models. For this particular station, two depth intervals within the crust emerge as the locations of steeper velocity gradients; one occurs at about 11 km depth, and another between the depths of about 35–38 km. The resulting profiles for all 27 SEAL3 stations are summarized in the second column cluster of Table 2. Along with the Moho depth estimates, the uncertainty and the nature of the transition from the crust to the mantle are also provided.

2.4 Rayleigh wave group velocity dispersion from ambient noise

The SEAL3 deployment provides a large volume of high-quality continuous records for durations in excess of 9 months. We computed the cross-correlation of the ambient noise wavefield on the vertical component of all simultaneously recording station pairs. The resulting time-averaged cross-correlograms exhibit a dispersed wave train (Fig. 6; left), which can be interpreted as the Rayleigh wave component of the Green's function of the intervening medium between the two stations (for more details, see Arroucau *et al.* (2010)).

The path-averaged group velocity for Rayleigh wave fundamental mode was obtained for periods ranging from 1 to 20 s for each station pair by means of the frequency-time analysis scheme introduced by Dziewonski *et al.* (1969). Low-quality data was then discarded based on the signal-to-noise ratio criterion described by Bensen *et al.* (2007). For large earthquakes, we can often observe surface waves with our short-period instruments because of the fact that reduced sensitivity at longer periods is offset by the large amplitudes of the waves. The fact that we can see 20 s surface waves is quite remarkable, but not unprecedented. For example, Arroucau *et al.* (2010) and Young *et al.* (2011) exploited the emergence of signal at these longer periods using the same instruments.

Our goal is to invert for shear wave velocity models from simultaneous modelling of RFs and surface wave dispersion curves. However, RFs are discrete points in geographical space as they are related to the location of single stations, although surface wave

Table 2. Results for the depth of Moho beneath SEAL3 stations, with uncertainties and the nature of sharpness from three different techniques used in this study: (1) grid-search modelling (columns 4–6), (2) inversion of RFs (columns 7–9) and (3) joint inversion of RFs and the Rayleigh wave dispersion data estimated from ambient noise (columns 10–12).

Station name	Station latitude	Station longitude	Moho depth grid-search	Uncer-tainty	Nature	Moho depth inversion	Uncer-tainty	Nature	Moho depth joint inversion	Uncer-tainty	Nature
S3A2	−32.88	146.74	–	>10	Gradual	–	>10	Gradual	–	>10	Gradual
S3A3	−32.89	147.3	35	3	Sharp	35	6	Medium	35	6	Medium
S3A4	−32.88	147.86	38	3	Sharp	37	4	Medium	35	6	Medium
S3A5	−32.91	148.49	29	3	Gradual	29	6	Gradual	27	4	Medium
S3A6	−32.90	148.91	36	3	Sharp	37	2	Sharp	39	4	Sharp
S3A7	−32.88	149.5	44	3	Gradual	39	8	Gradual	41	>10	Gradual
S3B1	−33.44	146.26	38	3	Medium	38	4	Medium	38	6	Medium
S3B5	−33.37	148.44	41	3	Sharp	41	2	Sharp	41	4	Sharp
S3B6	−33.35	148.92	47	3	Medium	41	10	Gradual	38	8	Gradual
S3B8	−33.33	149.99	38	3	Gradual	38	4	Medium	37	6	Gradual
S3C1	−33.84	146.25	35	3	Sharp	37	8	Gradual	38	>10	Gradual
S3C3	−33.85	147.3	32	3	Medium	32	5	Gradual	34	6	Medium
S3C5	−33.83	148.45	35	3	Gradual	31	5	Medium	30	6	Gradual
S3C7	−33.80	149.46	38	3	Sharp	38	2	Sharp	38	6	Sharp
S3C8	−33.82	150.01	–	>10	Gradual	–	>10	Gradual	–	>10	Gradual
S3C9	−34.05	150.50	39	3	Sharp	35	4	Medium	39	8	Medium
S3D2	−34.37	146.81	38	3	Medium	38	3	Medium	39	6	Medium
S3D7	−34.33	149.46	36	3	Sharp	36	2	Sharp	37	3	Sharp
S3E3	−34.86	147.35	41	3	Gradual	41	8	Gradual	44	8	Gradual
S3E5	−34.86	148.46	39	3	Medium	41	3	Medium	43	8	Medium
S3E7	−34.83	149.46	44	3	Medium	43	5	Gradual	44	5	Gradual
S3E8	−34.81	149.95	38	3	Sharp	40	4	Medium	38	4	Medium
S3F1	−35.44	147.06	38	3	Sharp	38	2	Sharp	39	5	Sharp
S3F2	−35.40	147.83	44	3	Sharp	45	8	Gradual	48	>10	Gradual
S3F3	−35.39	148.43	44	3	Sharp	43	3	Medium	45	>10	Gradual
S3G0	−36.04	147.68	35	3	Gradual	40	2	Sharp	40	8	Medium
S3G2	−35.99	149.04	47	3	Sharp	47	6	Gradual	53	4	Sharp

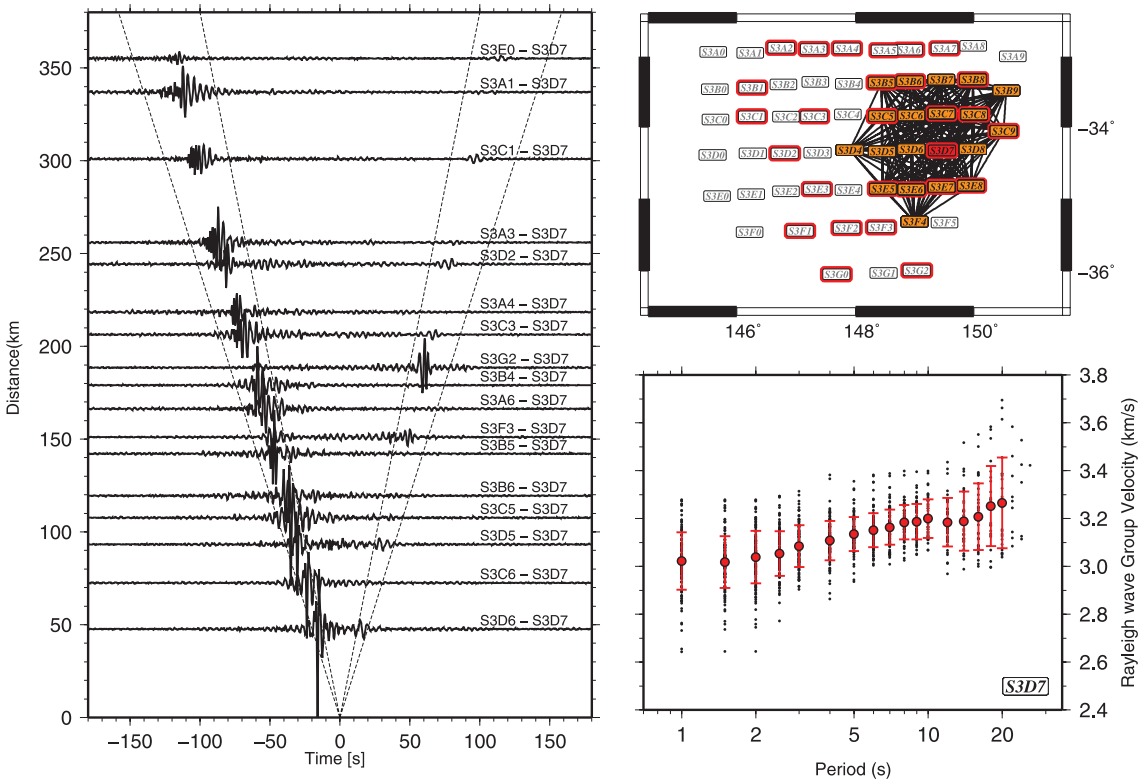

Figure 6. Record sections (left) showing raw cross-correlations between station S3D7 and neighbouring stations of the SEAL3 network. The apparent asymmetry between the causal and acausal arrivals of the Rayleigh wave is most likely caused by the vicinity to the coast. Actual dispersion estimate includes all station pairs surrounding, but excluding S3D7 (top right). Average group velocity measurements for S3D7 (bottom right), with error bars representing one standard deviation of the range of velocities at various periods.

dispersion curves derived from ambient noise processing are related to station pairs. Therefore, to relate a dispersion curve to each station for which a RF was available, we adopted the following strategy.

We selected the station pairs located within a radius of 150 km around the station of interest and calculated an average dispersion curve from all the group velocity measurements performed in that area, along with its corresponding standard deviation (Fig. 6, bottom right). The average velocities were only calculated if more than 20 observations were available for a given period. Although, it could be argued that shorter distances would constrain the local velocity field more accurately, our interest in periods up to 20 s to constrain the velocity field at greater depths imposes larger interstation distances. Average velocity dispersion curves were thus obtained and inverted simultaneously with RFs to infer 1-D velocity models beneath each station.

The group velocity tomography results (Arroucau *et al.* 2010) would also be useful in combination with RFs, however, estimating dispersion curves based on sample points taken exactly at the station location over a wide range of period suffers from some deficiencies. For example, there is no convincing method to estimate measurement errors for a given period, that is, there are no reliable bounds on the uncertainties associated with the group velocity from tomographic maps. Although not ideal, one possibility is to average tomographic velocities in a given area centred on the stationcoordinates. We compare dispersion curves estimated from tomography and from raw data in Fig. 7 for station S3D7 and find no significant difference for the periods of interest. Small error bars at higher periods for the estimates from tomography do not necessarily reflect that the uncertainty is small—they reflect the imposed smoothness and

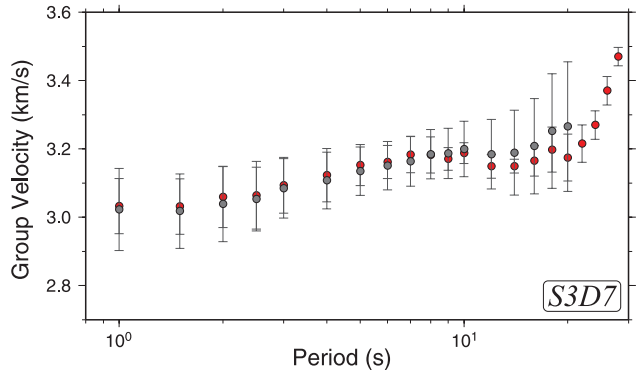

Figure 7. Average group velocity measurements for S3D7 (grey circles) from this study (see Fig. 6) compared with the estimates derived from the tomographic map of Arroucau *et al.* (2010) (red circles). In the former case, error bars represent one standard deviation of the range of velocities at various periods. In the latter case, the error bars represent the standard deviation associated with the average velocity in the corresponding squared area (100 km × 100 km centred on the station coordinates).

poorly resolved lateral variations. Sharp velocity gradients between two stations will not be well recovered by either method (when obtaining dispersion curves from unprocessed data, this is because of averaging; when obtaining dispersion curves from tomography, this is because of smoothing). As with station S3D7, we find no significant differences between the two methods for other analysed stations. Furthermore, we find that the inversion results based on using the dispersion curves from these two different methods differ

only by a negligible amount. In this respect, our direct measurements of surface wave dispersion curves from ambient noise are reliable, although ambient noise data sample relatively shallow depths. The advantage of our approach is that tomography does not need to be performed as a precursor to the joint inversion in order for it to work.

2.5 Linearized inversion for a detailed lithospheric structure (Steps 3 and 5)

We choose one of the best fitting grid-search models described in the previous section as a starting model for a linearized, iterative inversion. This approach inevitably increases the number of model parameters, hence sacrificing the simplicity of the initial structural models, yet it significantly improves RFs fits. We use the algorithm developed by Ammon (1997), which is based on singular value decomposition, to compute the matrix inverse and solve the inverse problem. The algorithm allows the use of smoothness parameters to find the smoothest solution in the vicinity of the initial model that fits the data.

We do not want to overparametrize our model space by a large number of layers. Here, we mitigate this problem by running a simple grid-search, in which we vary the number of iterations and the smoothness parameter in the inversion for different combinations of layers, as shown in Tkalčić *et al.* (2011). For station S3A4, there is an improvement in VR when increasing the number of layers from 6 to 10, much less improvement when going from 12 to 14 layers, and literally no improvement when increasing the number of layers to 16 or more. Therefore, the saturation in the improvement of the goodness-of-fit occurs when the number of layers is about 14. We repeat this procedure for each station, and, based on empirical results, we select an ensemble of models for three different sizes (numbers of layers), for smoothness parameters 0.1, 0.2 and 0.3 and for iterations from 10 to 50, to represent models with a good fit. More heavily smoothed models fail to reproduce the complexity in RFs. This process results in 360 models for each station, which are shown in orange in Figs 8 and 9. To compute the average velocity profiles, we have to perform additional discretization of layers to 1-km thickness. Our preferred model is computed as an average of all models in an ensemble. The preferred model (shown in red) is an arithmetic mean and appears as a model consisting of a large number of layers of 1-km thickness. However, note that the large number of layers is not a result of an overparametrization in the model space, but simply a result of our final representation

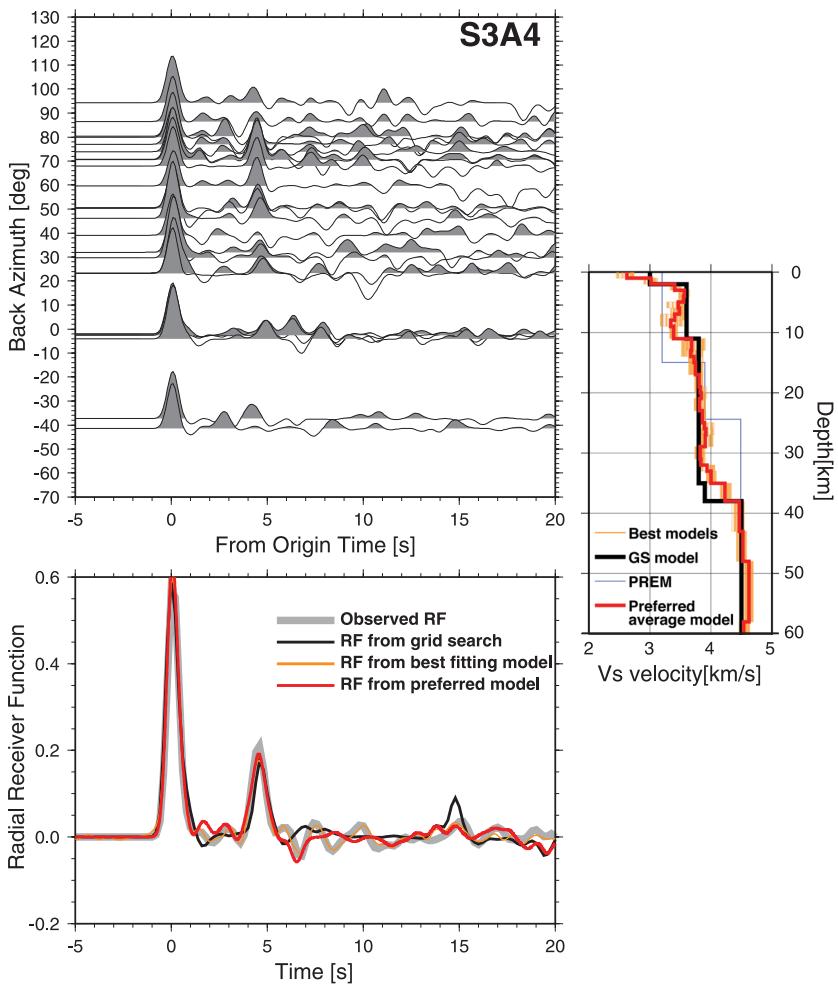

Figure 8. An example that shows results of modelling of Earth structure after Step 3 based only on the observed RFs. A record section of the selected observed RFs with respect to backazimuth for station S3A4 is shown in top left. Best models fitting the observed RFs (orange), and the preferred *S*-wave velocity model (red) are shown in top right. The starting model obtained from IRFFM2 and grid-search modelling (Steps 1 and 2; Fig. 5) as well as model PREM are shown in black and blue for comparison. The observed receiver function obtained from the cross-correlation matrix method, as described in the text, is shown with grey thick line (bottom). Also shown are the fits from the grid-search model (black), best-fitting model (orange) and our preferred model (red).

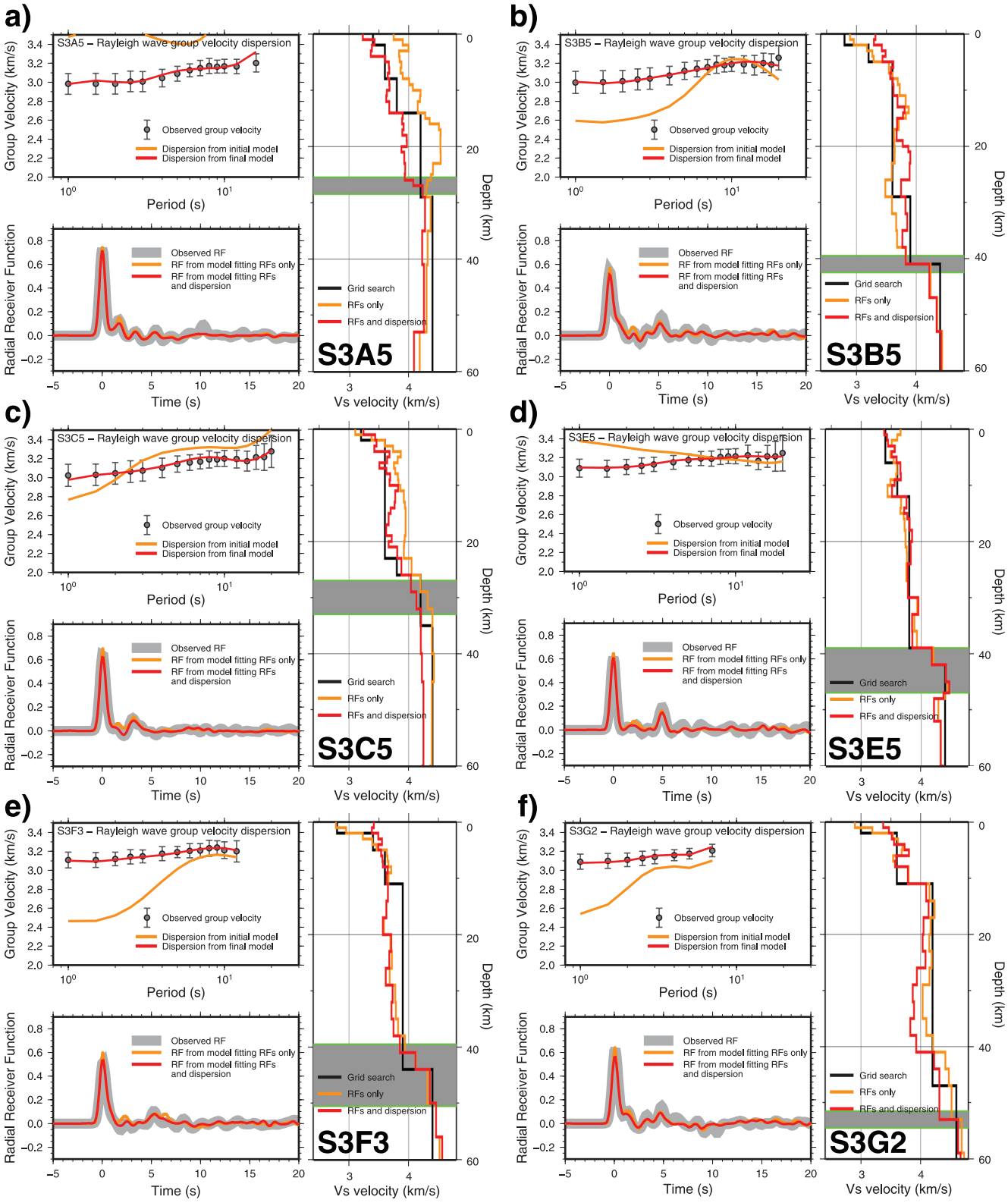

Figure 9. Resulting fits to the observed data (RFs shown with thick grey lines and dispersion shown with diamonds and error bars), and corresponding depth profiles of *S*-wave velocity obtained after Step 5 of the multistep modelling of RFs and ambient noise dispersion (red lines). Selected SEAL3 stations closely follow the north–south line: (a) S3A5, (b) S3B5, (c) S3C5, (d) S3E5, (e) S3F3 and (f) S3G2. Starting model obtained after IRFFM2 (Step 1) and grid-search modelling (Step 2) is shown with black. Preferred *S*-wave profiles from modelling of RFs only (Step 3; see example in Fig. 6) and fits to the observed data are shown with orange. The centre of the grey horizontal bar is the estimated position of Moho. All profiles are shown in Fig. 10.

of the preferred model. Although a single model from an ensemble might be the best-fitting model, it is not necessarily the best physical model. Note that, although the preferred model does not produce the best fit to the observed RFs (Fig. 8), it is a more likely representation of realistic Earth structure. Fig. 8 reveals that our preferred model for station S3A4 after Step 3 is indeed very similar to the model derived from the grid-search (Fig. 5, and the thick black line in Fig. 8), but more refined. The positions of the main gradients essentially do not change, but the Moho is more gradual and gives an impression of a slightly thinner crust. In addition, adding more layers results in lower velocities near the surface. The results after Step 3 for all 27 SEAL3 stations are summarized in the third column cluster of Table 2. In comparison with the grid-search results (Step 2), the crustal thickness remains very similar at the majority of considered stations, with the most notable change from 47 to 41 km for station S3B6. However, the nature of the discontinuity changes at 15 of 27 stations, which is not surprising given that the grid-search approach gives very limited sharpness estimates.

The grid-search and linearized inversion results described above provide good constraints on the depths in the crust at which the main gradients should occur, but still a poor idea about the absolute velocity. Therefore, the Rayleigh wave group velocity dispersion data is needed to calibrate the absolute velocity in 1-D models without significantly changing gradients as a function of depth (to preserve the fit required by RFs). At this point, IRFFM2 could be used again to help avoid a potential bias towards an unrealistic starting model, which is often the case where there are no other geophysical constraints on the area of study. We discuss IRFFM2 and Step 4 in Section 2.2, and show an example of interactive joint modelling in Fig. 4.

Armed with an already reasonable knowledge about the *S*-wave velocity changes as a function of depth beneath 27 SEAL3 stations, we approach the final step of our modelling (Step 5) in which we simultaneously invert RFs and ambient noise dispersion data. For the joint inversion, we use a program developed in Computer Programs in Seismology, Version 3.30 (Hermann 2002). Our results are as follows: (i) the absolute velocity shifts in comparison with the models determined in previous steps are significant and in some cases dramatic, (ii) the resulting 1-D profiles confirm the depths of the steepest gradients (discontinuities) determined from previous steps and do not reveal new discontinuities and (iii) our results emphasize the importance of having at least two complementary geophysical data sets to prevent non-uniqueness of the solutions.

Fig. 9 is a summary of our solutions for six selected stations of SEAL3. The stations for this figure are selected in such a way that they roughly follow a profile in a north–south direction (see Fig. 1). It is difficult to find a more complete profile, because of the fact that a number of the SEAL3 stations were too noisy to produce reliable RF results. This profile is thus a representative profile for SEAL3, as it consists of the stations that are located in the transition from the Murray Basin to the foothills of the Southern Highlands, and at least two stations in the mountainous area. Station S3A4, located strictly in the basin relatively far from the foothills, has already been featured in Fig. 5. Station S3B5 has been used in Fig. 4, and it is instructive to compare Fig. 4 with the results shown in Fig. 9(b).

First, the most striking result shown in Fig. 9 is the fact that the models derived from RFs only (shown with orange lines) represent a very poor fit to the Rayleigh wave dispersion data. Only for station S3C5, and, somewhat, for S3E5, do the models derived from RFs data predict the Rayleigh wave dispersion well. In all other cases, the predictions either overestimate the *S*-wave velocities (S3A5) or significantly underestimate the *S*-wave velocities (S3B5, S3F3 and S3G2). This means that even with the most careful approach in modelling RFs, we should limit our interpretation to the derived gradients in elastic properties, and refrain from making more profound conclusions about the absolute velocity beneath each station. Second, our final models (shown with red lines) fit both data sets well and are thus far more reliable and complete pieces of information about crustal structure than the models derived from only RFs. In some cases, the differences in the models are drastic and increase constraints on the Moho position (e.g. S3A5), although in some cases the differences are subtle, but still improve the fit to the dispersion data (e.g. S3E5, S3F3). It is sometimes enough for velocity near the surface to be modified to significantly improve the fit to the dispersion data, but in some cases, the changes are more complex because of the fact that the sensitivity kernels of surface wave dispersion consist of both positive and negative contributions (depending on Earth structure).

In general, the velocity profiles tend to change in terms of absolute velocity to accommodate the dispersion data, but without significant alterations in their overall shape as a function of depth (e.g. S3G2, S3C5). This is evident in the majority of the profiles for all 27 stations. The full assessment of the fits for all SEAL3 stations is not shown here because of space considerations. However, we show final velocity profiles for all stations in Fig. 10. The relative position of the velocity profiles in Fig. 10 corresponds to their grid locations (compare with Fig. 1). We interpret the Moho with a grey horizontal bar, whose thickness corresponds to the uncertainty. The more gradual the transition from the crust to the mantle, the greater the uncertainty. The results are summarized in the last quarter of Table 2. The depth to the Moho is given, together with the uncertainty and the nature of the transition (i.e. gradual, medium or sharp). The most notable change in the position of the Moho in comparison with the results from Step 3 is the increase in crustal thickness at station S3G2 from 47 to 53 km. The difference occurring at other stations are mostly confined to 1–2 km. The nature of the transition is changed at only 6 of 27 stations.

3 LITHOSPHERE BENEATH THE CENTRAL AND SOUTHERN NEW SOUTH WALES

3.1 Results

Multiple geophysical data sets were used to construct the crustal thickness, and crustal velocity profiles for 27 temporary stations in southeast Australia. To aid the interpretation of our results, the 5 s Rayleigh wave group velocity map of the region (Arroucau *et al.* 2010) is shown in Fig. 11. A comparison of the interpolated maps of crustal thickness (Moho depth) from different data sets is shown in Fig. 12. The results for four depth intervals, corresponding to the near surface (0–5 km depth), upper crust (5–10 km depth), middle crust (10–20 km depth) and lower crust (20–30 km depth), are shown in Fig. 13. For a given depth range, the average velocity beneath each station is calculated, and a laterally continuous velocity slice is obtained using the same interpolation procedure as that used for the Moho (Fig. 12). We organize the results of our multistep modelling into groups based on which profile they belong to (Profiles A–G in SEAL3—see Fig. 1). Such a division is somewhat arbitrary, but is used for convenience in discussion. We start from the north (A) and progress towards the south (G).

Profile A yielded results for six stations, at which we were able to extract both RFs and the ambient noise dispersion data. Only

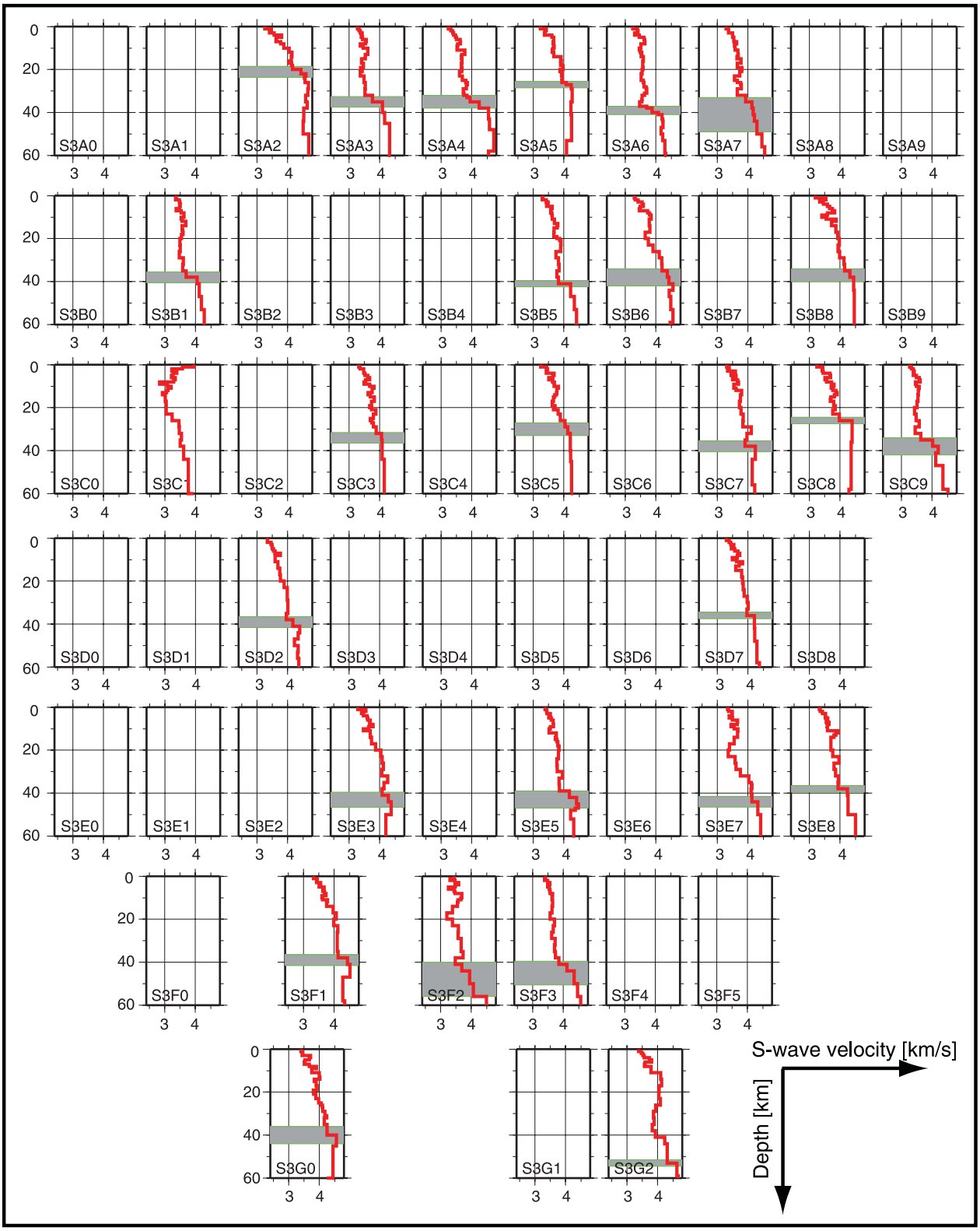

Figure 10. Resulting *S*-wave velocity profiles from multistep joint inversion of RFs and Rayleigh wave dispersion from ambient noise of all SEAL3 stations (including stations without estimated profiles due to large uncertainties in data). Relative position of profiles corresponds to their grid locations (compare with Fig. 1). The centre of the grey horizontal bar is the estimated position of Moho, and its thickness is the estimated uncertainty (compare with Table 2).

© 2012 The Authors, *GJI*, **189,** 1681–1700
Geophysical Journal International © 2012 RAS

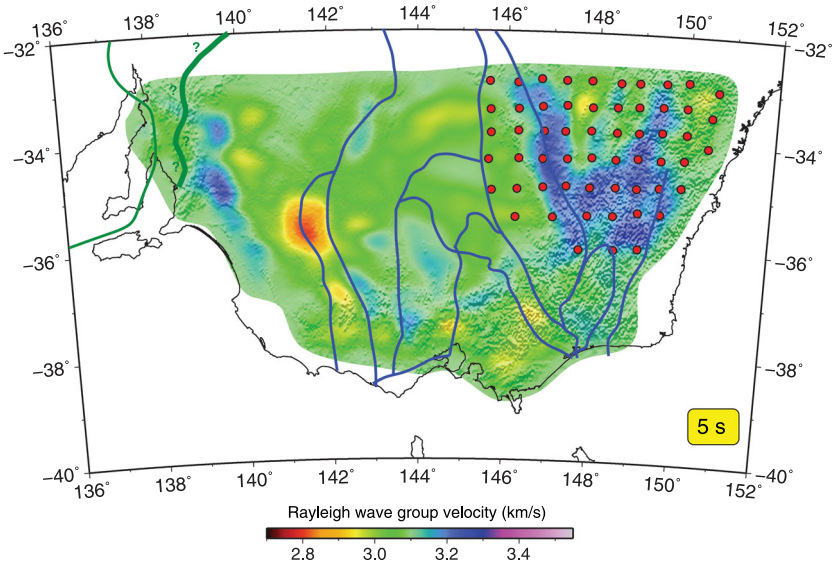

Figure 11. Group velocity map for the 5-s period after Arroucau *et al.* (2010) derived from the ambient seismic wavefield recorded by seven selected subarrays of the WOMBAT experiment (including SEAL3). The thick blue lines denote the tectonic boundaries shown in Fig. 2, the thick green line denotes the possible location of the Tasman Line and the thin green line denotes the approximate edge of the Gawler Craton. The red dots denote the locations of the SEAL3 stations.

for stations to the far west-end and for those to the far east-end of the profile were we unable to compute RFs. Station S3A2 has low velocities in the upper crust that display a gradual increase with depth, and is characterized by a pronounced transition to mantle-like velocities at a depth of about 23–24 km. Interestingly, this transition becomes clearer with the inclusion of the ambient noise dispersion data. However, this transition may not represent the base of the crust. We do not have reflection profiles that exactly overlay the location of this station, but there are peculiar features in the crust in the reflection profiles slightly to the west of S3A2. It is impossible to determine the depth to the Moho at this station because of a featureless nature of the depth profile, and we omit it from the Moho topography map featured in Fig. 12. Stations S3A3 and S3A4 show good agreement, particularly in the near-surface velocity profiles and at the Moho depths of about 35 km. These stations have among the highest quality RFs in our study, however, their profiles are very different from the neighbouring profile corresponding to the above mentioned S3A2 station. Furthermore, our estimate for the depth of the Moho at station S3A5 is 27 km (see also Fig. 9a). This is a rare example of a station where the profiles change drastically after adding the ambient noise dispersion data, although this is not surprising as the Moho is not very pronounced and RFs modelling does not yield a robust solution. Station S3A6 has a relatively sharp Moho at a depth of about 39 km. It is a robust feature in all inversion methods that we used. Upon adding the ambient noise dispersion data, the velocity profile changes significantly only in the upper crust as RFs alone yield velocities that are too low. Station S3A7 has a similar profile to S3A6, but the Moho is gradual, has a much larger uncertainty (more than 10 km) and, possibly, is positioned slightly deeper than at station S3A6. A relatively deep Moho in comparison with other stations along Profile A is not surprising given the fact that S3A7 is located in a mountainous region. In summary, if our interpretation of velocity-depth profiles at these stations is correct, the depth of the Moho in this region changes significantly across a length scale of about 50 km (the distance between two neighbouring stations) and it is comparable to the most rapid changes seen anywhere on the continent.

Profile B yielded results for four stations. Unfortunately, among those stations, only S3B5 and S3B6 are neighbouring, and allow direct comparison. Station S3B1 has a mildly pronounced, but relatively deep Moho (about 38 km). Although it is located in a basin, as Fig. 1 shows, it is close to higher topography in comparison with the neighbouring stations to the north. Stations S3B5 (featured in Figs 4 and 9b) and S3B6 show a reasonably good agreement, but station S3B6 has a less pronounced (more gradual) Moho. Interestingly, they both display a mid-crustal discontinuity at about 20 km depth, which is, again, sharper for station S3B5. A well defined low-velocity layer in the upper crust and a gradual Moho are evident in the refraction line data (Finlayson *et al.* 1980), although that line ran roughly parallel and near to our Profiles D and E. There was another refraction line running south from S3A6 to S3E6 to S3F4 (Finlayson *et al.* 2002). It shows a division between middle-lower crust at a depth of 20 km in the north, which thickens to the south, and then thins again. Finally, station S3B8 has a gradual Moho at a depth of about 37 km, in good agreement with the neighbouring stations available from Profile A. Modelling for this particular station requires a narrow low-velocity zone in the upper crust, at a depth of about 10 km.

The westernmost station along Profile C, station S3C1 is difficult to interpret. It has a pronounced low-velocity zone in the upper crust and gradually increasing velocities with depth without a clear indication of the Moho position. Based on the results of all three independent methods, the Moho might be as deep as 38 km, but the uncertainty is greater than 10 km. Station S3C3 has a gradual Moho at a depth of about 34 km. Interestingly, the profiles for this station are very different with and without the inclusion of the ambient noise dispersion data. This might be explained by the fact that the observed RF for this station is relatively featureless, hence containing less robust constraints on the position of discontinuities. Station S3C5 is featured in Fig. 9(c). The observed RF is somewhat similar to that observed at station S3C3, and so is the velocity profile, although the Moho lies a bit shallower (30 km). S3C7 has a relatively sharp and robust Moho at 38 km, found by all three independent methods. The crust appears to be void of discontinuities

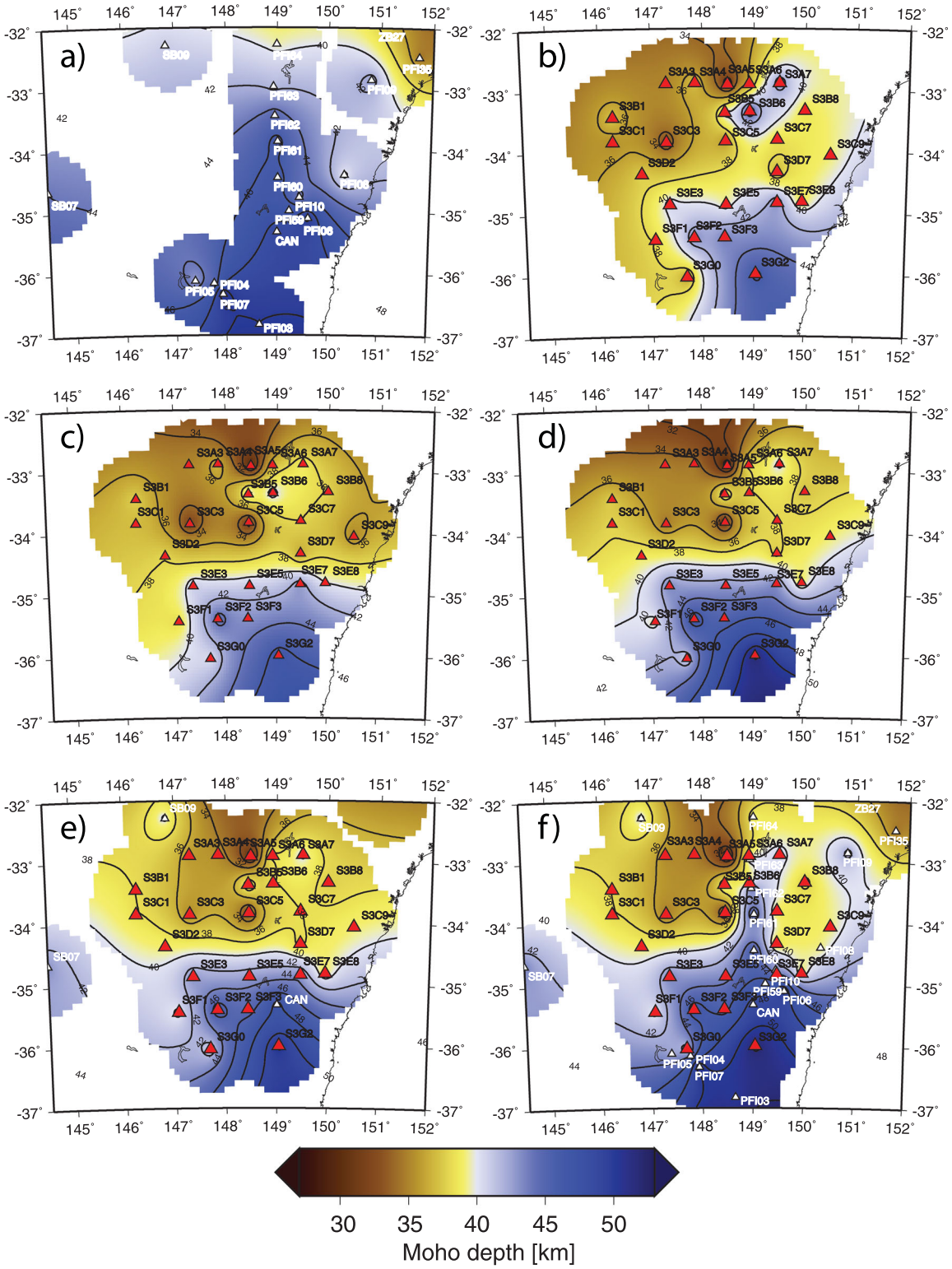

Figure 12. Comparison of interpolated maps of crustal thickness (Moho depth) from different datasets: (a) Moho depth from Collins *et al.* (2003) (COL) including Clitheroe *et al.* (2000) (CLI) and Shibutani *et al.* (1996) (SHI) data; (b) Moho depth from grid-search (Step 2); (c) Moho depth from linearized inversion (Step 3); (d) Moho depth from joint inversion of RFs and ambient noise Rayleigh wave dispersion curves (Step 5); (e) same as (d) including CLI and SHI points and (f) same as (d) including COL, CLI and SHI points.

with gradually increasing velocities from the surface to the mantle transition. The results indicate a discontinuity at a depth of 26 km. Although it is located at the edge of the mountainous region near the border with the Sydney Basin, we believe that this discontinuity corresponds to local variations in the crust and not to the base of the crust. There is no pronounced gravity anomaly in this area that would imply rapid changes in crustal thickness. A relatively sharp gradient in the crust is needed to explain the observed RF,

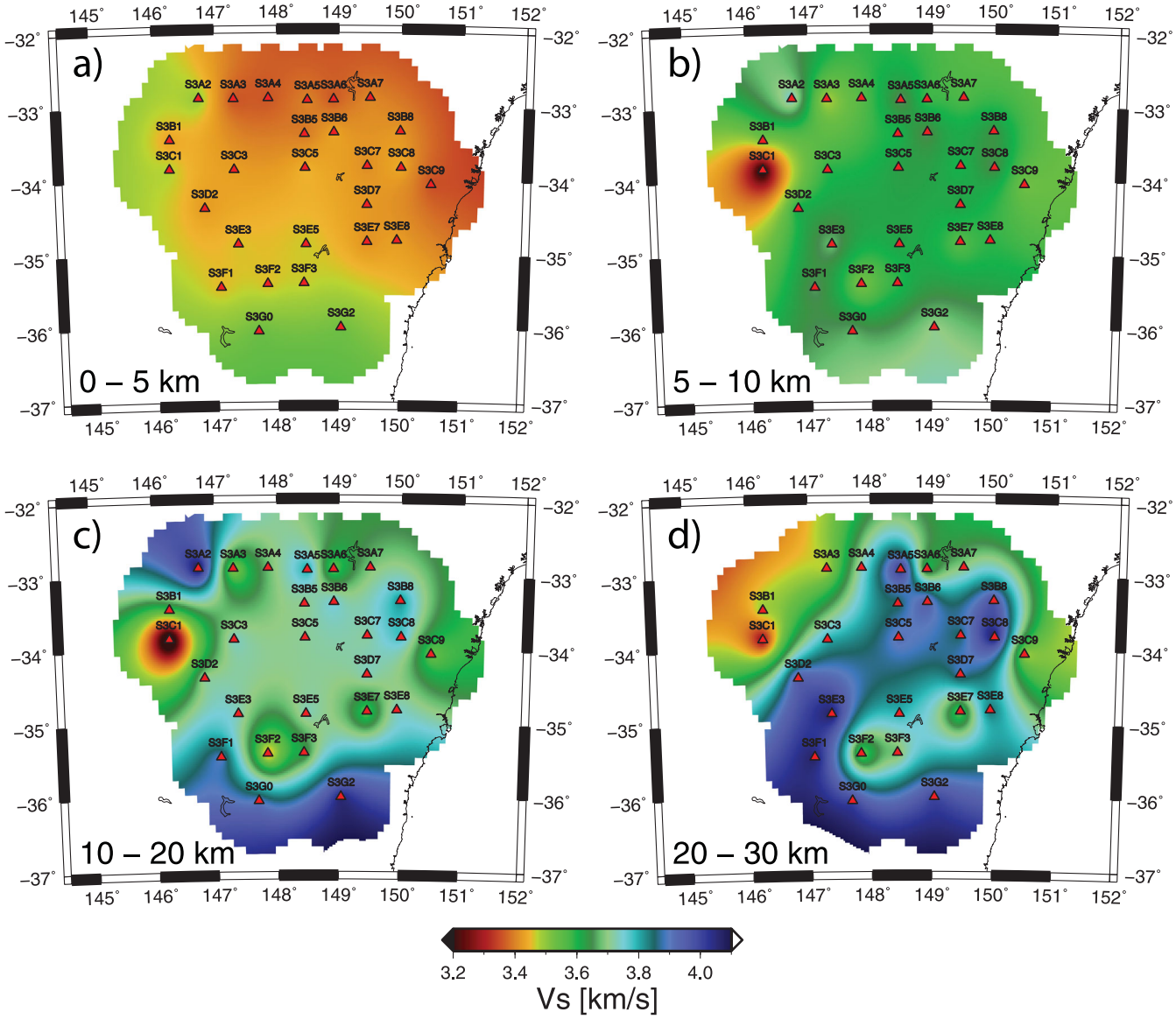

Figure 13. Comparison of interpolated maps of *S*-wave velocity at different depths: (a) 0–5 km; (b) 5–10 km; (c) 10–20 km and (d) 20–30 km.

however upon careful examination of individual RFs at this station, we concluded that their quality is low in comparison with the surrounding stations and thus we exclude this station from the Moho topography map featured in Fig. 12. Based on a gradual transition between the crust and the mantle at station S3C9, we placed the depth to the Moho at 39 km for this station. It should, however, be kept in mind that the uncertainty for this station is 8 km, and that the Moho could, in reality, lie as shallow as 34–35 km depth. Although, we initially found a very low-velocity layer near the surface from RFs modelling, when the ambient noise dispersion data were added, this confirmed velocities as high as for the majority of other stations. As a result, the resulting velocities are slightly higher in the upper crust and lower in the lower crust, which emphasizes the transition to the mantle, and the Moho could, arguably, be described as 'sharp'.

Profile D, unfortunately, yielded results for only two stations: S3D2 and S3D7. As we do not have results for any station in the middle of the profile, we omit a station from this profile from Fig. 9. RFs available at both stations, however, are of a good quality, and the depth of the Moho is a robustly determined feature from all three independent methods. When the ambient noise dispersion data are not considered, RFs modelling underestimates crustal velocities beneath station S3D2. The velocity profile with depth is characterized by a monotonic increase of velocities in the crust and a gradual to sharp transition to mantle velocities at a depth of about 39 km. Station S3D7 has a slightly more complicated profile, but a very distinct Moho at 37 km depth. A minor discontinuity in the upper crust occurs at about 15 km. RFs determine structure beneath S3D7 robustly without addition of the dispersion data, that is the velocity profile needs just a slight adjustment to fit the ambient noise dispersion data.

Along profile E, we successfully modelled four stations. Station S3E3 has notably higher velocities in the upper crust, as evidenced by the ambient noise dispersion data. RFs alone tend to underestimate velocities in the upper crust and overestimate them in the lower crust. The velocity profile with depth looks similar to that of station S3D2 in the north. We interpret the Moho as a gradual transition occurring at about 44 km depth. Another less significant discontinuity

is possible at a depth of about 33 km. Station S3E5 has a velocity profile that all three methods agree on. The Moho appears as a relatively sharp feature at a depth of 43 km, but because it has a step, we characterize it in Table 2 as 'gradual'. There is another discontinuity at a depth of 12 km, below which *S*-wave velocity remains constant throughout the crust. Station S3E7 has a more complex profile than S3E5, manifested in a pronounced low-velocity zone culminating at a depth of 20 km. The Moho is present as a gradual transition from the crust to the mantle at a depth of about 44 km. At station S3E8, rather conservatively, we characterize the Moho as a gradual transition between the crust and the mantle, but only relative to other stations (see, for comparison, stations S3B5 or S3C8, with sharp crust–mantle transitions). Apart from a robustly determined Moho at a depth of 44 km, there is another sharp discontinuity in the upper crust at a depth of 11 km, similar to that observed beneath station S3B5. The above mentioned refraction line (Finlayson *et al.* 1980) ran roughly parallel and near to SEAL3 Profiles D and E. Main results from that study are: (1) the Moho varies between 40 and 52 km depth; (2) velocity changes within the crust and at the Moho are transitional rather than discontinuous; (3) a well defined low-velocity layer is evident at about 15–20 km depth and (4) *S*-wave velocities are 3.65 km s^{-1} in the upper crust and 3.9 km s^{-1} in the lower crust.

Along Profile F, station S3F1 has a sharp Moho at a depth of about 39 km. The *S*-wave velocity profile beneath this station looks rather similar to that of other stations to the north located near the Palaeozoic boundary, as inferred from the map in Fig. 2 (S3D2 and S3E3). *S*-wave velocity increases monotonically in the upper crust and remains constant in the lower crust. Station S3F2 has a very different *S*-wave velocity profile with depth than station S3F1: most notably, absolute velocities throughout the crust are low. More complex variations of velocity in the upper crust are accompanied by a low-velocity zone culminating at a depth of 20 km (similar to S3E7). Moho occurs as a very broad transition with a very high uncertainty in depth. We report 48 km in Table 2, but Moho could be as deep as 56 km beneath this station. The ambient noise dispersion data significantly corrects absolute velocities for this station, although the overall shape of the *S*-wave velocity profile with depth does not change with the inclusion of the dispersion data. In comparison, station S3F3 has a very simple profile of slightly increasing *S*-wave velocities with depth and we interpret Moho to be centred at a depth of 45 km, although it appears as a broad and smooth transition and could extend well below 45 km. The inclusion of the ambient noise dispersion data increases velocities in the surface layer, but the rest of the velocity profile with depth remains almost unchanged.

Along the southernmost profile, Profile G, we were able to analyse two stations. In terms of absolute velocities, S3G0 looks more similar to S3F1 than to S3F2, with an additional jump in velocities in the uppermost crust at a depth of about 8 km. Moho occurs at a depth of about 40 km and is a relatively well-pronounced transition, although we conservatively assign an uncertainty of 8 km. Interestingly, if station S3A2 in the north-western corner of the array had the shallowest Moho, then the station in its south-eastern corner, S3G2, appears to have the deepest Moho of all analysed stations. Station S3G2 also has a very interesting *S*-wave velocity as a function of depth. Although, Moho stands out as a relatively sharp discontinuity, the *S*-wave velocity profile with depth is characterized by another, even sharper discontinuity, at a depth of 11 km. Not a single of the active-source study profiles coincides very accurately with station S3G2. Finlayson *et al.* (2002) indicate a *P*-wave discontinuity of around 0.4 km s^{-1} at the depth of around 15 km, but this is slightly north from S3G2. Finlayson *et al.* (1980) hint at variations at around 10 km depth, but again, this does not overly the S3G2 location.

Deeper than this discontinuity, there is a gradual decrease in velocity and a mildly pronounced low-velocity zone peaking at the depth of about 37–38 km. The gradient below this depth becomes positive and sharper, and terminates at Moho. The addition of the ambient noise dispersion data adjusts absolute velocity in the *S*-wave velocity profile slightly, but the overall shape of the profile remains the same with or without the inclusion of the dispersion data.

4 DISCUSSION AND CONCLUSIONS

We analysed RFs using the interactive forward-modelling software IRFFM2 featured in this manuscript for the first time, a grid-search and a linearized inversion via a multistep modelling scheme. To complement information from the observed RFs on the gradients in elastic parameters, and to increase constraints on absolute velocity structure, we used ambient noise dispersion data.

Our results demonstrate the importance of using multiple geophysical data sets in revealing 1-D *S*-wave velocity profiles. The differences in the obtained *S*-wave velocity profiles in terms of their overall shape with and without the inclusion of the ambient noise dispersion data are in most cases insignificant. However, in terms of absolute values, there are several cases in which the differences are significant and even dramatic. The main difference in the recovered profiles is because of the different sensitivity of RFs (more sensitive to gradients in elastic properties) and Rayleigh wave dispersion (more sensitive to absolute velocities). We start with modelling the RFs, and when the dispersion data is included via a simultaneous inversion scheme, changes in absolute velocities are apparent. Had we started with fitting the dispersion data first, and added the RFs data in a later stage of modelling, the resulting models would have not changed significantly in terms of absolute velocities but the newly obtained models would have revealed the position of main gradients with depth, therefore, the improvement would have appeared very significant. However, the depth resolution of the dispersion data is poor, and assumptions would have to be made as to how to smooth the 1-D models together to create a 3-D image. When the two data sets are simultaneously inverted, the resulting models improve upon previous constraints on Moho in this region, and the thickness of the crust constrained by several independent techniques used in this paper appears to vary significantly over the area of our study.

The SEAL3 deployment spans a large portion of the Eastern Subprovince of the Lachlan Orogen, and encroaches into the Central Subprovince to the west (Figs 1 and 2). At the western and eastern ends of the array, a number of stations also overlie the Murray and Sydney basins, respectively. Most of the eastern-half of the array also overlies the Southern Highlands (see Fig. 1), with the highest station at an elevation of 1490 m. A comparison between the Moho map shown in Fig. 12 and the topographic relief (Fig. 1) shows a broad general agreement between regions of increased elevation and regions of increased Moho depth, which is consistent with the presence of a substantial crustal root beneath the south-eastern highlands. Short scale-length variations in Moho depth are much more evident beneath the northeast sector of the array than elsewhere, which may be partly a function of data quality and the assumptions inherent to the method. However, given the robustness of the results, it appears that a purely Airy isostatic model is not appropriate to this region of the south-eastern highlands. It is interesting to note that

the northward change in character of the Moho beneath the southeast highlands occurs at approximately the boundary between the Snowy Mountains to the south and the Blue Mountains region to the north (between Profiles D and E). The lack of conformity between the Moho beneath the Blue Mountains region and the topographic relief may reflect significant lateral changes in composition, lithospheric strength and the mode of landscape development and rates of denudation on rifted margins (van der Beek *et al.* 2001).

The inferred change in the Palaeozoic basement between the Central and Eastern subprovinces is almost mimicked at the surface by a change from Cambrian–Devonian rocks exposed in the Southern Highlands, to Tertiary–Quaternary sediments in the Murray Basin (see Fig. 2). Inspection of the 1-D shear wave models in Fig. 10 does not reveal any pronounced shallow low-velocity zones beneath any of the stations that overlie the Murray Basin, which might indicate the presence of thick sediments. However, this is not particularly surprising because the Murray Basin is relatively thin, and the sediments are consolidated. In terms of Moho geometry, we do not observe any significant change in the shear wave models between stations that lie in the Central Subprovince and those that lie in the Eastern Subprovince, although one could argue that the Moho depths are less variable in the Central Subprovince. However, this observation is probably best explained by the absence of topography in this region.

Ambient noise tomography of southeast Australia has been carried out by Arroucau *et al.* (2010) using seven subarrays of WOMBAT, including SEAL3. Fig. 11 shows a 5 s Rayleigh wave group velocity map of the region with the SEAL3 stations superimposed. The change from higher velocities beneath the Eastern Subprovince to lower velocities beneath the Murray Basin is probably largely because of the crystalline rocks of the south-eastern highlands, exposed from deep within the crust by uplift and denudation, contrasting with lower velocity rocks which underpin the Murray Basin sediments. Given that the exposed portion of the Omeo Metamorphic Complex comprises metamorphosed Ordovician quartz-rich turbidites (Morand 1990), the basement of the Murray Basin is likely to be composed of sedimentary or metasedimentary rocks. The velocities at the near-surface (Fig. 13a) decrease gradually towards the northeast of the array, probably as a result of the Sydney Basin, and also the low velocity anomaly in the neighbourhood of station S3A4 that is also present in the ambient noise tomography result (see Fig. 11). As noted above, the presence of the Murray Basin is not evident in the joint inversion results. Although, the variation from higher group velocities in the east to lower group velocities in the west shares some degree of similarity with the shear wave velocity in Fig. 13, of the stations that produced results, it is indeed only S3B1 and S3C1 that lie emphatically in the Western Subprovince. The *S*-wave velocity profiles beneath both these stations exhibit lower average velocities than those to the east, and in fact S3C1 has particularly low mid-crustal velocities. However, this is not necessarily inconsistent with the results from surrounding stations: for instance in the lower crust (20–30 km depth), where the contribution from station S3A2 has been removed because of the shallowness of the Moho, it appears that there is a broad negative velocity gradient to the northwest. Although, this result appears at odds with the S3A2 RF, it could be reconciled if dipping layers within the crust separate regions of similar velocity.

Compared to the near-surface and upper crust, a different pattern of velocity anomalies becomes evident at greater depths. In the mid-lower crust, a broad zone of elevated velocities is present beneath the Blue Mountains northwest of Sydney. This zone extends southwest beneath stations S3E3 and S3F1, before curling east beneath S3G0 and S3G2, thus leaving the region in the neighbourhood of S3F2, S3F3, S3E5, S3E7 and S3E8 as a low-velocity zone. Given that this pattern of anomalies does not mimic the Moho (Fig. 12), it is unlikely to be an artefact of velocity-interface depth trade-off. Interpretation is a challenge, because the surface geology provides no obvious insights, and previous studies using ambient noise data (Arroucau *et al.* 2010) and teleseismic tomography (Rawlinson *et al.* 2011) do not constrain the lower crust. In a recent surface wave tomography study (Fishwick *et al.* 2008), it was found that the lithosphere thins in a series of discrete steps towards the eastern margin of the Australian continent, with recent Cenozoic volcanism concentrated near the coast where the lithosphere is thinnest (as little as 50 km thick). It is likely that the lateral variations in mid-lower crustal velocity that we observe reflect the complicated interactions of a thinning lithosphere, associated igneous underplating, recent hotspot-related volcanism and uplift. However, in the absence of additional data from seismic and other sources, it is not possible to provide a definitive interpretation of velocity variations in the lower crust.

Other individual features observed in the final *S*-wave velocity profiles (Fig. 13) and localized variations in Moho topography (Fig. 12) could reflect local crustal structure around individual stations, but it would be too ambitious at this point to relate them to broader tectonic concepts. The multistep approach in modelling RFs and surface wave dispersion presented here is time consuming, but we recommend it over traditional one-step inversion approaches, as each step gives a better insight and understanding of the modelling process, and reveals additional details of Earth structure. The results presented here were augmented with other independent geophysical data sets, and they were used in assembling together individual pieces in a considerably refined image of the Australian crust (Kennett *et al.* 2011). They will also be used in correcting for near-surface structure and constraining the depth of the Moho in teleseismic tomography, as well as in removing long wavelength information from gravity data.

ACKNOWLEDGMENTS

AK's internship was sponsored from the ARC discovery grant DP0986750. PA is supported by National Science Foundation CREST award HRD-0833184. The maintenance of the instruments and the collection and handling of short-period data was performed by members of the Seismology Group of the Research School of Earth Sciences, in, very often, difficult field conditions, and we gratefully acknowledge their contribution. We would like to thank the authors of Generic Mapping Tools (GMT) Wessel & Smith (1998). We also thank C. Ammon for making his iterative inversion code available, B. Herrmann for making available Computer Programs in Seismology and C. D. N. Collins for providing the depths to the Moho from previous work. We are grateful to an anonymous reviewer for a constructive review that improved the manuscript.

REFERENCES

Agostinetti, N.P., Lucente, F.P., Selvaggi, G. & Di Bona, M., 2002. Crustal structure and Moho geometry beneath the northern Appennines (Italy), *Geophys. Res. Lett.,* **29**(20), doi:10.1029/2002GL015109.

Ammon, C.J., 1991. The isolation of receiver effects from teleseismic P waveforms, *Bull. seism. Soc. Am.,* **81,** 2504–2510.

Ammon, C.J., 1997. Receiver-function inversion; software and manual. Available at: http://eqseis.geosc.psu.edu/~cammon/HTML/RftnDocs/rfinv01.html (last accessed 2012 March 25).

Ammon, C.J., Randall, G.E. & Zandt, G., 1990. On the non-uniqueness of receiver function inversions, *J. geophys. Res.,* **95,** 15 303–15 318.

Arroucau, P., Rawlinson, N. & Sambridge, M., 2010. New insight into Cainozoic sedimentary basins and Palaeozoic suture zones in southeast Australia from ambient noise surface wave tomography, *Geophys. Res. Lett.,* **37,** L07303, doi:10.1029/2009GL041974.

Baker, G.E., Minster, B., Zandt, G. & Gurrola, H., 1996. Constraints on crustal structure and complex Moho topography beneath Piñon Flat, California, from teleseismic receiver functions, *Bull. seism. Soc. Am.,* **86,** 1830–1844.

Bensen, G.D., Ritzwoller, M.H., Barmin, M.P., Levshin, A.L., Lin, F., Moschetti, M.P., Shapiro, N.M. & Yang, Y., 2007. Processing seismic ambient noise data to obtain reliable broad-band surface wave dispersion measurements, *Geophys. J. Int.,* **169,** 1239–1260.

Betts, P.G., Giles, D., Lister, G.S. & Frick, L.R., 2002. Evolution of the Australian lithosphere, *Aust. J. Earth Sci.,* **49,** 661–695.

Birch, F., 1961. The velocity of compressional waves in rocks to 10 kilobars, Part 2, *J. geophys. Res.,* **66,** 2199–2224.

Çakir, Ö., Erduran, M., Çinar, H. & Yilmaztürk, A., 2000. Forward modelling receiver functions for crustal structure beneath station TBZ (Trabzon, Turkey), *Geophys. J. Int.,* **140,** 341–356.

Cassidy, J.F., 1992. Numerical experiments in broadband receiver function analysis, *Bull. seism. Soc. Am.,* **82,** 1453–1474.

Cayley, R.A., Taylor, D.H., van den Berg, A.H.M. & Moore, D.H., 2002. Proterozoic—Early Palaeozoic rocks and the Tyennan Orogeny in central Victoria: the Selwyn Block and its tectonic implications, *Aust. J. Earth Sci.,* **49,** 225–254.

Chang, S.-J., Baag, C.-E. & Langston, C.A., 2004. Joint analysis of teleseismic receiver functions and surface wave dispersion using the genetic algorithm, *Bull. seism. Soc. Am.,* **94,** 691–704.

Chen, Y., Niu, F., Liu, R., Huang, Z., Tkalčić, H., Sun, L. & Chan, W., 2010. Crustal structure beneath China from receiver function analysis, *J. geophys. Res.,* **115,** B033067, doi:10.1029/2009JB006386.

Chevrot, S. & van der Hilst, R.D., 2000. The Poisson ratio of the Australian crust: geological and geophysical implications, *Earth planet. Sci. Lett.,* **183,** 121–132.

Clitheroe, G., Gudmundsson, O. & Kennett, B.L.N., 2000. The crustal thickness of Australia, *J. geophys. Res.,* **105,** 13 697–13 713.

Collins, C.D.N., 1991. The nature of the crust-mantle boundary under Australia from seismic evidence, in *The Australian Lithosphere, Vol. 17 of Special Publication,* pp. 67–80, ed. Drummond, B.J., Geological Society of Australia Incorporated, Sydney.

Collins, C.D.N., Drummond, B.J. & Nicoll, M.G., 2003. Crustal thickness patterns in the Australian continent, *Geol. Soc. Aust. Spec. Publ.,* **22,** and *Geol. Soc. Am. Spec. Pap.,* **372,** 121–128.

Drummond, B.J. & Collins, C.D.N., 1988. Seismic velocities in the crust and upper mantle of Australia, Technical Report 277, BMR Report, Australian Government Publishing Services, Canberra.

Du, Z.J. & Foulger, G.R., 1999. The crustal structure beneath the northwest fjords, Iceland, from receiver functions and surface waves, *Geophys. J. Int.,* **139,** 419–432.

Dziewonski, A., Bloch, S. & Landisman, M., 1969. A technique for the analysis of transient seismic signals, *Bull. seism. Soc. Am.,* **59**(1), 427–444.

Dziewonski, A.M. & Anderson, D.L., 1981. Preliminary reference Earth model, *Phys. Earth planet. Inter.,* **25,** 297–356.

Finlayson, D.M., Collins, C.D.N. & Denham, D., 1980. Crustal structure under the Lachlan Fold Belt, southeastern Australia, *Phys. Earth planet. Inter.,* **21,** 321–342.

Finlayson, D.M., Korsch, R.J., Geln, R.A., Leven, J.H. & Johnston, D.W., 2002. Seismic imaging and crustal architecture across the Lachlan Transverse Zone, a possible early cross-cutting feature of Eastern Australia, *Aust. J. Earth Sci.,* **49,** 311–321.

Fishwick, S. Heintz, M., Kennett, B.L.N., Reading, A.M. & Yoshizawa, K., 2008. Steps in lithospheric thickness within eastern Australia, evidence from surface wave tomography, *Tectonics,* **27,** doi:10.1029/2007TC002116.

Foster, D.A. & Gray, D.R., 2000. Evolution and structure of the Lachlan Fold Belt (Orogen) of eastern Australia, *Annu. Rev. Earth planet. Sci.,* **28,** 47–80.

Foster, D.A., Gray, D.R., Spaggiari, C., Kamenov, G. & Bierlein, F.P., 2009. Palaeozoic Lachlan Oregon, Australia; accretion and construction of continental crust in a marginal ocean setting: isotopic evidence from Cambrian metavolcanic rocks, *Geol. Soc. Lond. Spec. Publ.,* **318,** 329–349.

Glen, R.A., 2005. The Tasmanides of eastern Australia, in *Terrane Processes at the Margins of Gondwana,* pp. 23–96, eds Vaughan, A.P.M., Leat, P.T. & Pankhurst, R.J., Geology Society, London.

Glen, R.A., Percival, I.G. & Quinn, C.D., 2009. Ordovician continental margin terranes in the Lachlan Orogen, Australia: implications for tectonics in an accretionary orogen along the east Gondwana margin, *Tectonics,* **28,** TC6012, doi:10.1029/2009TC002446.

Helffrich, G., 2006. Extended-time multitaper frequency domain cross-correlation receiver-function estimation, *Bull. seism. Soc. Am.,* **96,** 344–347, doi:10.1785/0120050098.

Hermann, R.B., 2002. Computer programs in seismology, current version 3.30; software and manual. Available at: http://www.eas.slu.edu/People/RBHerrmann/CPS330.html (last accessed 2012 March 25).

Julià, J., Ammon, C.J., Herrmann, R.B. & Correig, A.M., 2000. Joint inversion of receiver function and surface wave dispersion observations, *Geophys. J. Int.,* **143,** 1–19.

Julià, J., Ammon, C.J. & Herrmann, R.B., 2003. Lithospheric structure of the Arabian shield from the joint inversion of receiver functions and surface wave dispersion, *Tectonophysics,* **371,** 1–21.

Kennett, B.L.N., 1983. *Seismic Wave Propagation, Chapter 9 in Stratified Media,* Cambridge University Press, Cambridge.

Kennett, B.L.N., 1997. The mantle under Australia, *AGSO J. Aust. Geol. Geophys.,* **17,** 49–54.

Kennett, B.L.N. & Furumura, T., 2008. Stochastic waveguide in the lithosphere: Indonesian subduction zone to Australian Craton, *Geophys. J. Int.,* **172,** 363–382, doi:10.1111/j.1365-246X.2007.03647.x.

Kennett, B.L.N., Engdahl, B.E. & Buland, R., 1995. Constrains on the velocity structure in the Earth from travel times, *Geophys. J. Int.,* **122,** 108–124.

Kennett, B.L.N., Salmon, M., Saygin, E. & AusMoho Working Group, 2011. AusMoho: the variation of Moho depth in Australia, *Geophys. J. Int.,* **187,** 946–958, doi:10.1111/j.1365-246X.2011.05194.x.

Kind, R., Kosarev, G.L. & Petersen, N.V., 1995. Receiver functions at the stations of the German Regional Seismic Network (GRSN), *Geophys. J. Int.,* **121,** 191–202.

Knight, L.A., McDonald, P.A., Frankel, E. & Moore, D.H., 1995. A preliminary appraisal of the pre-Tertiary infrabasins beneath the Murray Basin, northwestern Victoria, *Victorian Initiative for Minerals and Petroleum Report*, **16,** Geological Survey of Victoria, Melbourne.

Langston, C.A., 1979. Structure under Mount Rainier, Washington, inferred from teleseismic body waves, *J. geophys. Res.,* **84,** 4749–4762.

Laske, G., Masters, G. & Rief, C., 2000. Crust 2.0, Available at: http://mahi.ucsd.edu/~gabi/crust2.html (last accessed on 2011 September 11).

Lawrence, J.F. & Wiens, D.A., 2004. Combined receiver-function and surface wave phase-velocity inversion using a niching genetic algorithm: application to Patagonia, *Bull. seism. Soc. Am.,* **94,** 977–987.

Ligorría, J.P. & Ammon, C.J., 1999. Iterative deconvolution and receiver function estimation, *Bull. seism. Soc. Am.,* **89,** 1395–1400.

Lister, G.S., Ethridge, M.A. & Symonds, P.A., 1991. Detachment models for the formation of passive continental margins, *Tectonics,* **10,** 1038–1064.

Mohorovičić, A., 1910. Potres od 8.X 1909. (Das Beben vom 8.X. 1909.), (Jahrbuch des meteorologischen Observatoriums in Zagreb (Agram) für das Jahr 1909), 1–56 (English translation, 1992. Earthquake of 1909 October 8, *Geofizika,* **9,** 3–55).

Morand, V.J., 1990. Low-pressure regional metamorphism in the Omeo Metamorphic Complex, Victoria, Australia, *J. Metamorph. Geol.,* **8,** 1–12.

Owens, T.J., 1987. Crustal structure of the Adirondacks determined from broadband teleseismic waveform modelling, *J. geophys. Res.,* **92,** 6391–6401.

Owens, T.J., Taylor, S.R. & Zandt, G., 1987. Crustal structure at regional seismic test network stations determined from inversion of broadband teleseismic P waveforms, *Bull. seism. Soc. Am.,* **77,** 631–632.

Özalaybey, S., Savage, M.K., Sheehan, A.F., Louie, J.N. & Brune, J.N., 1997. Shear-wave velocity structure in the northern basin and range province from the combined analysis of receiver functions and surface waves, *Bull. seism. Soc. Am.,* **87,** 183–189.

Park, J. & Levin, V. 2000. Receiver functions from multiple-taper spectral correlation estimates, *Bull. seism. Soc. Am.,* **90,** 1507–1520.

Pasyanos, M., Tkalčić, H., Gök, R. & Rodgers, A., 2007. Seismic structure of Kuwait from joint inversion of surface wave group velocities and RFs, *Geophys. J. Int.,* **170,** 299–312.

Phinney, R., 1964. Structure of the Earth's crust from spectral behaviour of long-period body waves, *J. geophys. Res.,* **69,** 2997–3017.

Price, R.C., Gray, C.M. & Frey, F.A., 1997. Strontium isotopic and trace element heterogeneity in the plains basalts of the Newer Volcanic Province, Victoria, Australia, *Geochim. cosmochim. Acta.,* **61,** 171–192.

Rawlinson, N. & Kennett, B.L.N., 2008. Teleseismic tomography of the upper mantle beneath the southern Lachlan Orogen, *Phys. Earth planet. Inter.,* **167,** 84–97.

Rawlinson, N., Kennett, B.L.N. & Heintz, M., 2006. Insights into the structure of the upper mantle beneath the Murray Basin from 3-D teleseismic tomography, *Aust. J. Earth Sci.,* **53,** 595–604.

Rawlinson, N., Tkalčić, H. & Kennett, B.L.N., 2008. New results from WOMBAT: an ongoing program of passive seismic array deployments in Australia, *EOS, Trans. Am. geophys. Un.,* **89**(53), Fall Meet. Suppl., Abstract S22A-03.

Rawlinson, N., Kennett, B.L.N., Vanacore, E., Glen, R.A. & Fishwick, S., 2011. The structure of the upper mantle beneath the Delamerian and Lachlan orogens from simultaneous inversion of multiple teleseismic datasets, *Gondwana Res.,* **19,** 788–799.

Reading, A.M., Kennett, B.L.N. & Sambridge, M., 2003. Improved inversion for seismic structure using transformed, S-wave vector RFs: removing the effect of the free surface, *Geophys. Res. Lett.,* **30,** doi:10.1029/2003GL018090.

Saito, M., 1988. DISPER80: a subroutine package for the calculation of seismic normal-model solutions, in *Seismological Algorithms,* pp. 294–319, ed. Doornbos, D.J., Academic Press, New York.

Sambridge, M., 1999. Geophysical inversion with a neighbourhood algorithm -II. Appraising the ensemble, *Geophys. J. Int.,* **138,** 727–746.

Sandvol, E., Seber, D., Calvert, A. & Barazangi, M., 1998. Grid-search modelling of receiver functions: implications for crustal structure in the Middle East and North Africa, *J. geophys. Res.,* **103,** 26 899–26 917.

Shibutani, T., Sambridge, M. & Kennett, B.L.N., 1996. Genetic algorithm inversion for receiver functions with application to crust and uppermost mantle structure beneath Eastern Australia, *Geophys. Res. Lett.,* **23,** 1829–1832.

Stipčević, J., Tkalčić, H., Herak, M., Markušić, S. & Herak, D., 2011. Crustal and upper mantle structure beneath the External Dinarides, Croatia determined from teleseismic receiver functions, *Geophys. J. Int.,* **185,** 1103–1119, doi:10.1111/j.1365-246X.2011.05004.x.

Taylor, D.H. & Cayley, R.A., 2000. Character and kinematics of faults within the turbidite-dominated Lachlan Orogen: implications for tectonic evolution of eastern Australia: discussion, *J. Struct. Geol.,* **22,** 523–528.

Tkalčić, H., 2011. Interactive Receiver-Functions Forward Modeller II; software and manual. Available at: http://rses.anu.edu.au/~hrvoje/IRFFMv1.1.html (last accessed 2012 March 25).

Tkalčić, H., Pasyanos, M., Rodgers, A., Gök, R., Walter, W. & Al-Amri, A., 2006. A multi-step approach in joint modelling of surface wave dispersion and teleseismic RFs: implications for lithospheric structure of the Arabian Peninsula, *J. geophys. Res.,* **111,** B11311, doi:10.1029/2005JB004130.

Tkalčić, H., Chen, Y., Liu, R., Huang, Z., Sun, L. & Chan, W., 2011. Multi-step modelling of teleseismic receiver functions combined with constraints from seismic tomography: crustal structure beneath southeast China, *Geophys. J. Int.,* **187,** 303–326, doi:10.1111/j.1365-246X.2011.05132.x.

van der Beek, P.A., Braun, J. & Lambeck, K., 1999. Post-Palaeozoic uplift history of southeastern Australia revisited: results from a process-based model of landscape evolution, *Aust. J. Earth Sci.,* **46,** 157–172.

van der Beek, P.A., Pulford, A. & Braun, J., 2001. Cenozoic landscape development in the Blue Mountains (SE Australia): lithological and tectonic controls on rifted margin morphology, *J. Geol.,* **109,** 35–56.

van der Hilst, R.D., Kennett, B.L.N., Christie, D. & Grant, J., 1994. SKIPPY: mobile broad-arrays to study the seismic structure of the lithosphere and mantle beneath Australia, *EOS, Trans. Am. geophys. Un.,* **75,** 177, 180 & 181.

Vinnik, L.P., 1977. Detection of waves converted from P to SV in the mantle, *Phys. Earth planet. Inter.,* **15,** 39–45.

Wessel, P. & Smith, W.H.F., 1998. New, improved version of the Generic Mapping Tools Released, *EOS, Trans. Am. geophys. Un.,* **79,** 579.

Wilde, S.A., Valley, J.W., Peck, W.H. & Graham, C.M., 2001. Evidence from detrital zircons for the existence of continental crust and oceans on the Earth 4.4 Gyr ago, *Nature,* **409,** 175–178.

Young, M., Rawlinson, N., Arroucau, P., Reading, A.M. & Tkalčić, H., 2011. High frequency ambient noise tomography of southeast Australia: new constraints on Tasmania's tectonic past, *Geophys. Res. Lett.,* **38,** L13313, doi:10.1029/2011GL047971.

Young, M., Tkalčić, H., Rawlinson, N. & Reading, A.M., 2012. Full waveform moment tensor inversion in a low seismicity region using multiple teleseismic datasets and ambient noise: application to the 2007 Shark Bay, Western Australia, earthquake, *Geophys. J. Int.,* **188,** 1303–1321 doi:10.1111/j.1365-246X.2011.05326.x.

Zhu, L. & Kanamori, H., 2000. Moho depth variation in southern California from teleseismic receiver functions, *J. geophys. Res.,* **105,** 2969–2980.